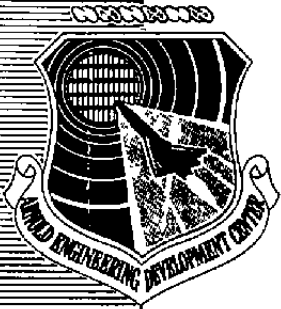C.2

Analytical Studies of
High-Pressure MHD Accelerators

G. L. Whitehead
ARO, Inc.

September 1981

Final Report for Period October 1, 1977 — September 30, 1978

ARNOLD ENGINEERING DEVELOPMENT CENTER
ARNOLD AIR FORCE STATION, TENNESSEE
AIR FORCE SYSTEMS COMMAND
UNITED STATES AIR FORCE

This report has been reviewed by the Office of Public Affairs (PA) and is releasable to the National Technical Information Service (NTIS). At NTIS, it will be available to the general public, including foreign nations.
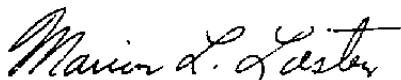
APPROVAL STATEMENT

This report has been reviewed and approved.

MARSHALL K. KINGERY
Directorate of Technology
Deputy for Operations

Approved for publication:

FOR THE COMMANDER

MARION L. LASTER
Director of Technology
Deputy for Operations

REPORT DOCUMENTATION PAGE		READ INSTRUCTIONS BEFORE COMPLETING FORM
1 REPORT NUMBER AEDC-TR-81-18	2 GOVT ACCESSION NO.	3 RECIPIENT'S CATALOG NUMBER
4 TITLE (and Subtitle) ANALYTICAL STUDIES OF HIGH-PRESSURE MHD ACCELERATORS		5 TYPE OF REPORT & PERIOD COVERED Final Report, Oct 1, 1977 to Sept 30, 1978
		6 PERFORMING ORG REPORT NUMBER
7 AUTHOR(s) G. L. Whitehead, ARO, Inc., a Sverdrup Corporation Company		8 CONTRACT OR GRANT NUMBER(s)
9 PERFORMING ORGANIZATION NAME AND ADDRESS Arnold Engineering Development Center/DOTR Air Force Systems Command Arnold Air Force Station, TN 37389		10 PROGRAM ELEMENT, PROJECT, TASK AREA & WORK UNIT NUMBERS Program Element 65807F
11 CONTROLLING OFFICE NAME AND ADDRESS Arnold Engineering Development Center/DOS Air Force Systems Command Arnold Air Force Station, TN 37389		12 REPORT DATE September 1981
		13 NUMBER OF PAGES 79
14 MONITORING AGENCY NAME & ADDRESS(if different from Controlling Office)		15 SECURITY CLASS (of this report) UNCLASSIFIED
		15a DECLASSIFICATION DOWNGRADING SCHEDULE N/A

16 DISTRIBUTION STATEMENT (of this Report)

Approved for public release; distribution unlimited.

17 DISTRIBUTION STATEMENT (of the abstract entered in Block 20, if different from Report)

18 SUPPLEMENTARY NOTES

Available in Defense Technical Information Center (DTIC)

19 KEY WORDS (Continue on reverse side if necessary and identify by block number)

magnetohydrodynamics (MHD)   electrical insulation
test facilities   magnetic fields
reentry vehicles
acceleration (MHD)
computers

20 ABSTRACT (Continue on reverse side if necessary and identify by block number)

An analytical study was made of the feasibility of using an MHD-augmented arc as the primary component of a large reentry vehicle test facility. Computer studies of the performance of MHD accelerator channels were made for systems having channel input power of 50 MW to 1,700 MW. It was determined that complete simulation of reentry conditions is not possible in a single extended-flow facility. The studies showed, however, that very

DD ,FORM 1473 EDITION OF 1 NOV 65 IS OBSOLETE
    1 JAN 73

20. ABSTRACT (Continued)

large increases in performance over existing arc facilities could be attained by use of MHD augmentation, provided, however, that several very difficult design problems could be solved. The most critical problem area was identified as that of maintaining the design integrity of the magnetic-field walls of the channel, which requires that a high level of electrical insulation be retained under a heating load of up to 10 kw/cm^2. Only a marked increase in high-temperature materials technology would permit the use of uncooled refractories for these walls. The possibility of using film cooling for these walls was explored and it was found that, in addition to a substantial increase in complexity, such an approach would result in significant reductions in performance and efficiency of the MHD channel.

AFSC
Arnold AFS Tenn

PREFACE

The work reported herein was conducted by the Arnold Engineering Development Center (AEDC), Air force Systems Command (AFSC). Gregory Cowley, First Lieutenant, USAF, was the Air Force project manager. The results presented in this report were obtained by ARO, Inc., AEDC Group (a Sverdrup Corporation Company), operating contractor for the AEDC, AFSC, Arnold Air Force Station, Tennessee. The work was done under ARO Project No. P32S-L4, and the manuscript was submitted for publication on November 10, 1978.

The author wishes to express his appreciation to Dr. Philip A. Kessel for his contribution of the film cooling portion of the report, and to Mr. Richard T. Smith, who has been involved in the Working Group since the Group's formation in 1973.

Mr. G. L. Whitehead is currently employed by Calspan Field Services, Inc., AEDC Division.

CONTENTS

ILLUSTRATIONS

TABLES

1.0 INTRODUCTION

It has been recognized for some time that existing ground test facilities are inadequate to perform the full range of tests required in the development of advanced missile and space vehicles. Indeed, technological trends have called for, even demanded, increased ground test capabilities for both military and space programs. In particular, the ever increasing performance criteria for missiles and reentry vehicles demand increasing test capabilities in the area of ablation, particle erosion, and coupled ablation/erosion of nosetips. Existing arc heater facilities do not permit full simulation of reentry conditions and existing ballistic ranges are inadequate to provide the required test times to acquire necessary nosetip shape change data.

Historically, ground test facilities have been developed or modified to meet the presently existing test requirements and, in general, the test requirements have increased before the facilities are fully operational, leaving the test capabilities continually lagging the technological requirements. Such a deficiency in reentry ground test capabilities led to the formation of the Joint Advanced Ballistic Re-Entry System/Arnold Engineering Development Center (ABRES/AEDC) Reentry Test Facility Working Group (hereinafter referred to as the working group) in November 1973 to investigate the feasibility of providing an improved ground test facility. The working group was comprised of representatives of AEDC, ABRES, and five other government agencies. The working group charter was, essentially, to investigate all potential test facility concepts, select the ones which appeared capable of providing the stringent test conditions, and perform detailed analytical and experimental investigations to determine the feasibility of developing a ground test facility capable of simulating all critical parameters of a reentry flight. After looking at all potential concepts, the guided-track range and the MHD accelerator were selected as the candidate facilities which warranted further investigation. The AEDC was assigned the responsibility of coordinating all tasks resulting from

the above charter and evaluating all studies performed in support of the effort. The work reported herein is a result of the working group studies and presents the results obtained from the detailed study of the feasibility of using an arc-driven MHD accelerator as the prime component of a large-scale ground test facility.

2.0 REQUIREMENTS FOR REENTRY VEHICLE GROUND TEST FACILITIES

2.1 GENERAL CONSIDERATIONS

Although the technological level has continually advanced, the role of ground test remains with the same basic goals which led to the first crude wind tunnels. Those goals include verification of analytical predictions wherein closely observed experiments give data which enhance the understanding of the basic hypothesis. Secondly, design information is always eagerly sought as various practical applications of basic principles are tested for validity under controlled conditions. Thirdly, ground test facilities provide a valuable tool for concept screening and, finally, generation of relative performance data provides a firm basis for evaluating candidate systems or components designed to benefit from the previously generated information. The role of ground testing, then, is critical to technology development and the rate of advancement of technology is largely dependent on how well ground test facilities fulfill their role. In the area of reentry technology, existing ground test facilities are deficient because the full conditions of reentry are not achieved and investigators are left with the necessity of piecemeal testing in many test units, each selected to meet specific requirements. Trimble, et al. (Ref. 1), address this situation and discuss several existing test facilities and the capability each has of meeting particular requirements. Even piecemeal testing, however, is not adequate to cover the full range in all areas of interest and researchers must still resort to repeated expensive flight test to generate an adequate base of information.

2.2 REENTRY TEST OBJECTIVE

A ballistic nose cone reentering the atmosphere will trace a path similar to that shown in Fig. 1, and the stringent conditions of various reentry trajectories are shown graphically in Fig. 2. The present trend is toward even higher performance and larger throw weights, both of which lead to increased heating rates on the vehicle nosetip. As a result, development efforts now center around developing ablative nosetip materials capable of surviving such environments. This determines the primary types of ground tests desired and they include: (1) nosetip ablation/shape change, (2) coupled nosetip and heat shield ablation/erosion, (3) nosetip thermostructural response, (4) aerodynamic testing of ballistic and maneuvering vehicles, (5) transpiration-cooled nosetip performance in heating/erosion environments, and (6) special tests such as control surface ablation. Those test objectives are listed in the presently conceived order of priority, and it appears that such a priority will hold for the foreseeable future. The envelope which a test facility would be required to cover to meet the test objectives is shown in Fig. 2 and repeated in Fig. 3. In Fig. 3, the existing test facility envelopes are shown as a function of stagnation pressure and stagnation enthalpy. The test time, which is the principal limitation of the ballistic range, is noted, but no mention is made of Mach number, which limits the arc facilities. An "ideal" facility would provide real time simulation of all critical parameters over the range encountered in an actual trajectory, and do so over a flow area commensurate with a full-size vehicle. The parameter simulation requirements of such a facility are listed in the middle column of Table 1.

The simultaneous achievement of the required pressure, enthalpy, Mach number, and test time listed in Table 1 is virtually impossible to attain in a ground test facility. The stagnation pressure and stagnation enthalpy must be reasonably well simulated if the mandatory high energy transfer rates are to be obtained. Mach number simulation is less important if it
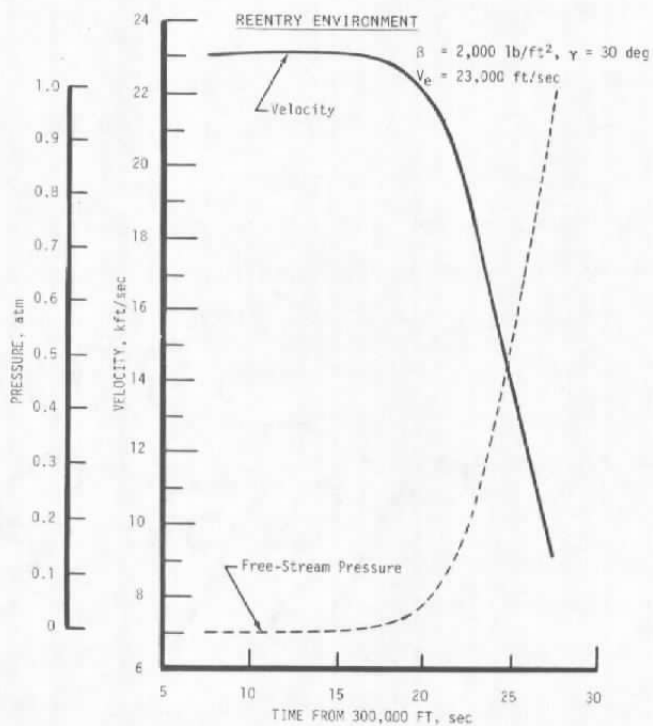
Figure 1. Typical ballistic reentry.
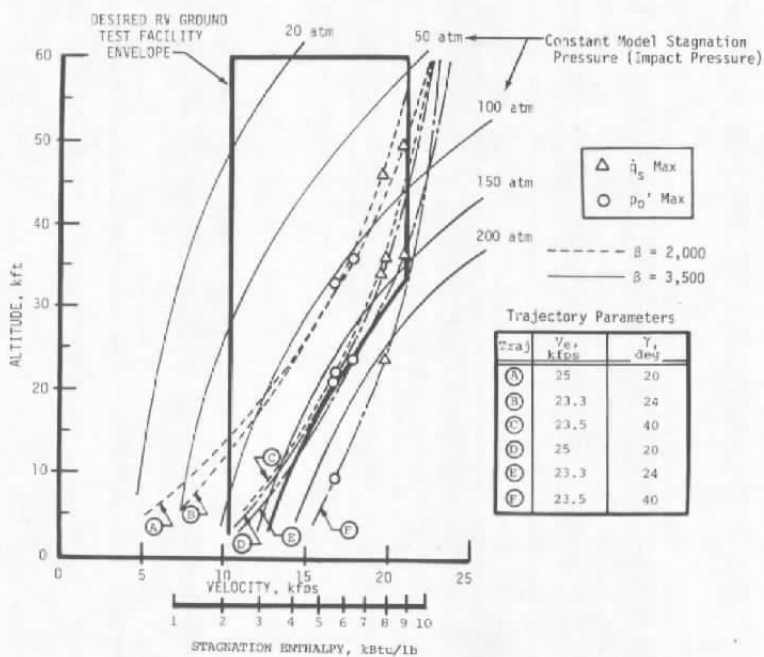
Figure 2. Typical reentry conditions.

10
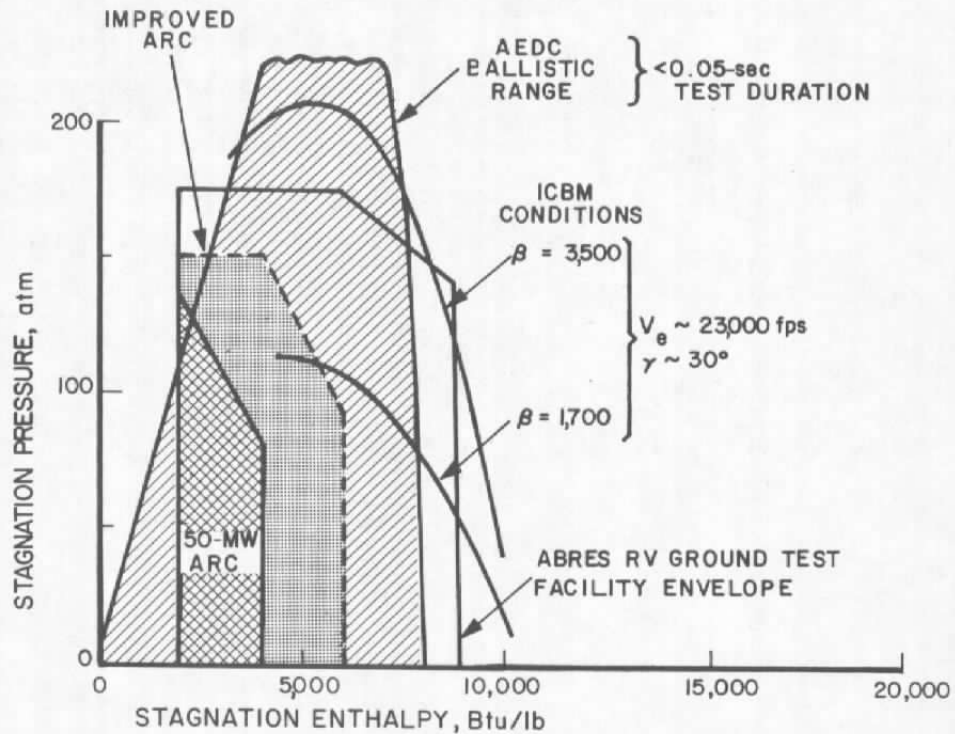
Figure 3. Stagnation pressure, enthalpy
requirement for reentry facility.

Table 1. Reentry Facilities Requirements

	Requirements	Minimum Acceptable
Mach No.	20	8
Stagnation Pressure, atm	200	170
Stagnation Enthalpy, Btu/lbm	8,000	8,800
Nosetip Diameter – Length, in.	4 diameter – 6 length	1.3 diameter – 2 length
Cone Base – Length, in.	25 base – 60 length	8.3 base – 20 length
Test Time, sec	30	10

2.6 in^2
246 in^2

$T \sim 18000 \, R$

$\langle c_p \rangle = \dfrac{8 \times 10^3}{1.8 \times 10^4} \doteq 0.44$

$H \sqrt{P} = 8800 \sqrt{170} \doteq 115,000$

11

is sufficiently high. Figure 4 shows the effect of Mach number on the pressure distribution of a sphere-cone, and Fig. 5 shows the relationship for turbulent heat flux distribution. It can be seen that an $M = 5$ flow would reasonably duplicate an $M = 20$ condition and considerable relaxation of that parameter is possible. However, other parameters, such as pitching moment and flap drag, are more sensitive to Mach number and hypersonic Mach numbers are required ($M \gtrsim 8$). The test time can also be relaxed, as can be seen from Fig. 1, so long as a significant fraction of the high-pressure portion of the trajectory is covered. Based on these considerations, the reduced requirements listed in Table 1 were deemed acceptable by the working group.
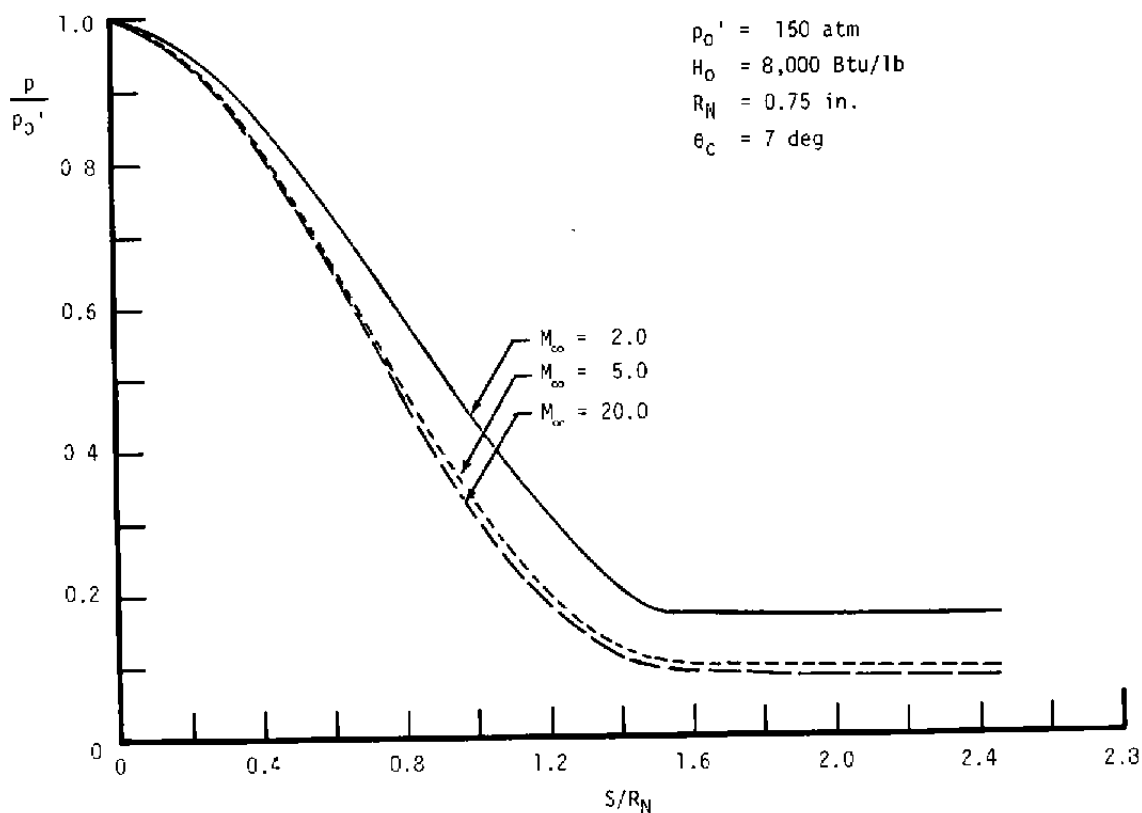
Figure 4. Influence of free-stream Mach number on pressure distribution on a sphere-cone.
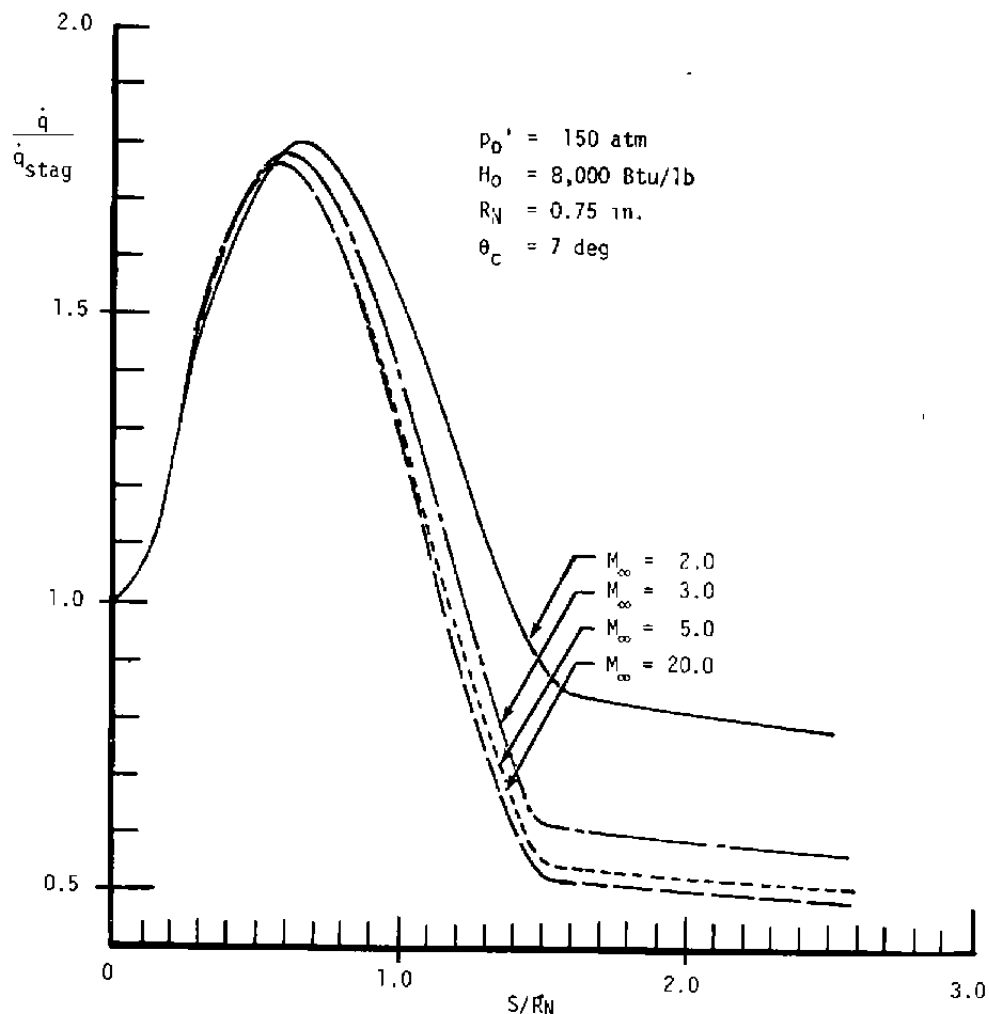
Figure 5. Influence of free-stream Mach number on
turbulent heat flux on a sphere-cone.

Derbidge and Wolf (Ref. 2) present an excellent discussion on reentry
facilities and their requirements. That report is also a result of the
working group studies and complements the present report.

3.0 FIXED-MODEL FACILITIES

3.1 GENERAL CONSIDERATIONS

Ground test facilities generally fall into two categories: (1) fixed
model/moving gas and (2) moving model/stationary gas. Arc facilities and

ballistic ranges (whether guided track or free flight) are prime examples
of each, respectively. The fixed-model concept has the advantage of long
test time, low operating cost, and superior measurement capability on the
model. The inherent disadvantages, when compared to a ballistic range,
are flow nonuniformities and uncertainty in the local conditions of the
flow itself. The major limitation for high-velocity, high-enthalpy flight
simulation in a static model facility, however, is the necessity to gener-
ate and contain a high-temperature, high-pressure gas and then expand this
plasma through a supersonic nozzle. The present state of the art places
definite upper limits on the pressure and enthalpy which can be contained
without container or nozzle failure. At present, these limits are well
below those required for hypersonic Mach number and flight impact pressure
simulation. For example, an M = 20 expanding flow with a model impact pres-
sure of 200 atm (Table 1) would require an isentropic stagnation pressure in
excess of 10^7 atm. If a nominal value of 200 atm arc heater reservoir pres-
sure is assumed as the current state of the art in arc heater technology,
then isentropic expansion to M = 8 would yield an impact pressure on the
model of only 0.25 atm. To attain impact pressures on the order of 100
atm would limit the Mach number to M ≈ 2. Figure 6 shows the stagnation
pressure which would be required to produce the acceptable flow parameters
in Table 1. Note that a stagnation pressure on the order of 400,000 atm ✻
would be required for an M = 8 flow with an impact pressure of 170 atm.
The inability to generate and contain these enormous pressures clearly
limits the conventional systems to very low Mach numbers.

An only slightly less formidable limitation of moving gas facilities
is the very large amount of power required to generate sustained hypersonic
flows of fairly modest dimensions. To simulate a given condition, the
energy which must be contained per unit stream volume is fixed only by the
velocity and altitude simulated; therefore, the energy requirement can be
generally applied to all moving gas concepts. The only variables are
the efficiency with which the energy is added and the source of the added
energy (i.e., chemical, electrical). If proper air chemistry is to be

✻ Gas Tables @ K = 1.2

14

achieved, chemical addition is forbidden, leaving only electrically powered airstreams to be considered. Figure 7 gives the power required in the gas to produce the desired simulation parameters in various size flow streams. As can be seen from that graph, the power level rapidly exceeds the installed capacity of most test installations.
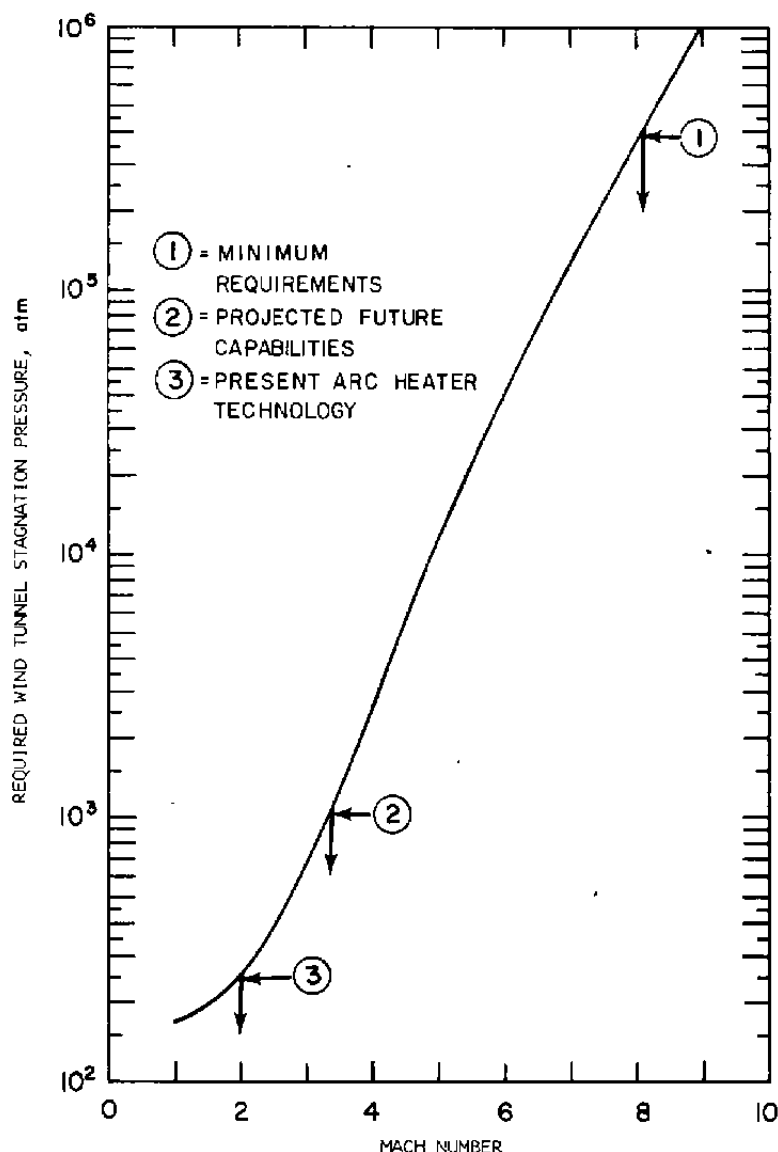
Figure 6. Wind tunnel stagnation pressure required for model stagnation pressure of 170 atm.

15

20,600
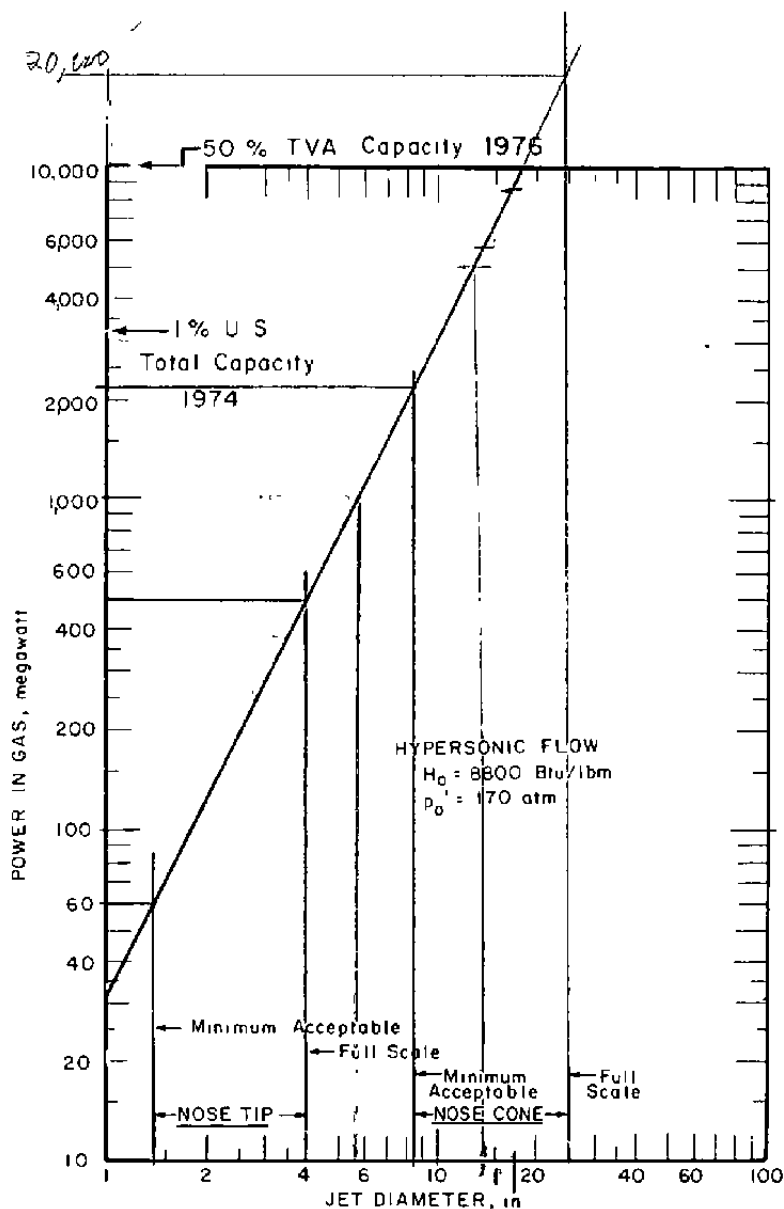
Figure 7. Power required for large
diameter ablation flows.

3.2 MHD-AUGMENTED FACILITIES

As stated previously, the power requirement applies equally to all
static model/moving gas facilities, and will be of prime consideration in
the development of a large-scale ground test facility of this type. The
power level, the method of energy addition, and the efficiency of energy
addition must all be considered in evaluating potential facility concepts.

However, if the basic assumption is made that adequate power can be provided, the point of energy addition becomes the more relevant consideration. By the addition of directed kinetic energy to a flowing gas downstream of a nozzle throat, the inherent limitation of conventional systems (generation, containment, expansion of high-pressure, high-enthalpy gases) can be effectively circumvented. In principle, such energy addition can be obtained by use of magnetohydrodynamic (MHD) forces. The feasibility of developing a usable test facility using an MHD accelerator is discussed in detail in the following sections.

4.0 REVIEW OF MHD ACCELERATORS

4.1 BASIC PRINCIPLES

Although MHD accelerators have been in existence for many years and reported extensively in the literature, a brief review of the fundamental principles is in order.

In an MHD accelerator, an ionized plasma is forced to flow through a channel contained in a magnetic field oriented at right angles to the flow direction. An electric current is forced to flow through the plasma at right angles to both the flow direction and the magnetic field. The interaction of the crossed fields will generate a body force on the charged particles in the flow. These charged particles will, in turn, collide with the neutral particles, thereby transmitting the force to the entire flow stream. The force per unit volume of this Lorentz force is equal to the vector product of the current density and the magnetic field strength, or $\vec{j} \times \vec{B}$.

Consider, then, the schematic of a typical accelerator shown in Fig. 8. Since it is fundamental to the operation of any MHD device that the working fluid must be an electrical conductor, the accelerator must have a plasma generator as a driver. Though other sources have not been eliminated, an arc heater has been assumed as the plasma generator for the present studies. Extensive development work and experimental testing was conducted on MHD

M ~ 2.0

M = 1.0

M < < 1.0

HIGH-ENERGY AIR HEATER

⊙ B

MAGNET

TEST SPECIMEN

−

TYPICAL OF EACH POWER SUPPLY

+

● HIGHER PRESSURES
● HYPERSONIC MACH NO.
● HIGH ENTHALPY
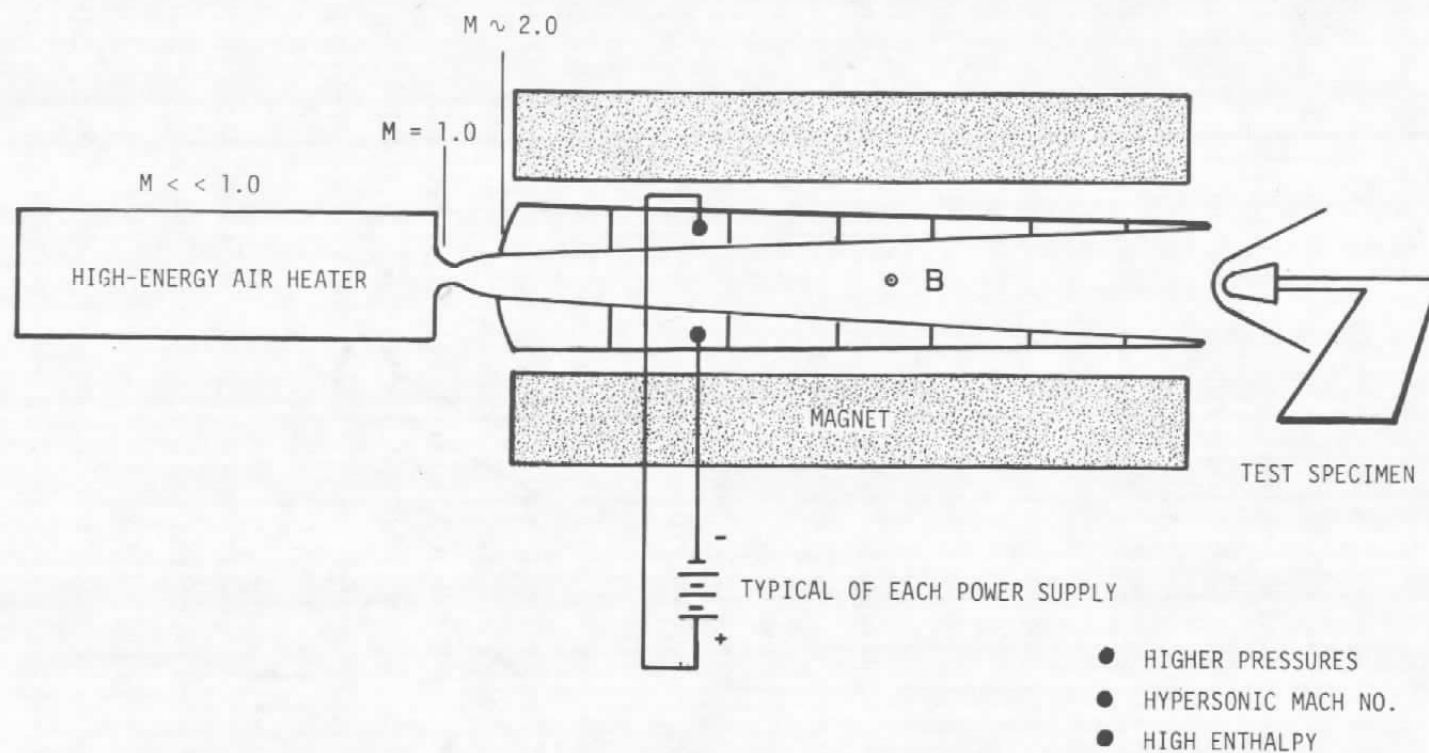
Figure 8. Typical MHD accelerator.

accelerators in the middle 1960's, with the major efforts being conducted at AEDC and NASA-Langley. The principle of MHD acceleration was demonstrated in those programs and the results have been extensively reported in the literature (Refs. 3, 4, and 5). Velocity increases on the order of two were demonstrated, but most of that work was conducted at atmospheric pressure levels or below and, in general, at input power levels less than 1 MW. In the present application, where it is required to produce impact pressures of 170 atm, preliminary ideal channel calculations indicate the MHD channel will have to operate at static pressures at least an order of magnitude greater (~ 20 atm), and this fact will have substantial influence on the operating configuration of the channel.

Since air has a quite high ionization potential, it will not supply sufficient free electrons to become a good conductor at reasonable static temperatures. For this reason the flow is seeded with small amounts of a substance which can be easily ionized, such as potassium or cesium. The resulting plasma is then expanded through a supersonic nozzle and enters the accelerator as a high-temperature, high-velocity plasma. The governing equations for the channel flow can be derived briefly as follows.

Consider a neutral, homogeneous plasma flowing in the presence of an applied magnetic field. The assumption that the plasma is homogeneous means that gradients in temperature, pressure, and specie composition which exist in the thermal boundary layer will be considered to be small and will be neglected as a first approximation. It is further assumed that the applied magnetic field is not affected by the currents in the channel and that the ion slip is negligible.

Now, the density of a current flowing in an ionized plasma is given by

$$\vec{j} = \sigma \, \vec{E}*$$ (1)

19

where E* is the effective driving field. For the case of an ionized plasma flowing in the presence of a magnetic field, there will be an induced voltage given by

$$\vec{E}_{ind} = \vec{u} \times \vec{B} \tag{2}$$

Then Eq. (1) becomes

$$\vec{j} = \sigma[\vec{E} + \vec{u} \times \vec{B}] \tag{3}$$

It can be shown that, because of the Hall effect, there is another term which must be considered. Namely, if there is an applied field in the y direction, $\vec{E}_y$, perpendicular to $\vec{B}$ there will be an electron drift velocity in the x direction given by

$$\vec{v}_{dx} = \frac{\vec{E}_y}{\vec{B}} \tag{4}$$

Likewise, an applied $\vec{E}_x$ causes an electron drift velocity in the y direction given by

$$\vec{v}_{dy} = \frac{\vec{E}_x}{\vec{B}} \tag{5}$$

Now, just as there was an induced field, $\vec{E}_{ind}$, caused by the plasma velocity interacting with a magnetic field, there is an induced field caused by the electron drift velocity. This is commonly called the Hall field, the components of which are given by

$$\vec{E}_{xH} = \vec{v}_{dy} \times \vec{B} \tag{6}$$

and

$$\vec{E}_{yH} = \vec{v}_{dx} \times \vec{B} \tag{7}$$

The flux of charges across unit area per unit time is the current density, j, and is related to the electron drift velocity by

$$\vec{j} = - n_e \, e \, \vec{v}_d \tag{8}$$

Using Eq. (8) and applying to $\vec{j}_x$ and $\vec{j}_y$ gives

$$\vec{j}_y = - n_e \, e \, \vec{v}_{dy} \tag{9}$$

and

$$\vec{j}_x = - n_e \, e \, \vec{v}_{dx} \tag{10}$$

Rearranging

$$\vec{v}_{dy} = - \frac{\vec{j}_y}{n_e \, e} \tag{11}$$

and

$$\vec{v}_{dx} = - \frac{\vec{j}_x}{n_e \, e} \tag{12}$$

Substituting Eqs. (11) and (12) into Eqs. (6) and (7) gives

$$\vec{E}_{xH} = - \frac{\vec{j}_y}{n_e \, e} \times \vec{B} \tag{13}$$

and

$$\vec{E}_{yH} = - \frac{\vec{j}_x}{n_e \, e} \times \vec{B} \tag{14}$$

In general, then, there is an induced Hall field given by

$$\vec{E}_H = - \frac{\vec{j}}{n_e e} \times \vec{B} \tag{15}$$

Since the Hall current produced by the Hall field acts to reduce the effective plasma conductivity, the field given in Eq. (15) will act to oppose the driving field in Eq. (3) as the sign indicates. Combining Eqs. (3) and (15) gives

$$\vec{j} = \sigma \left\{ \left[\vec{E} + \vec{u} \times \vec{B} \right] - \frac{1}{n_e e} \vec{j} \times \vec{B} \right\} \tag{16}$$

Thus, the driving force for the electrons is the combined electric and magnetic fields.

Equation (16) was derived assuming arbitrary directions for $\vec{u}$, $\vec{B}$, and $\vec{E}$. For normal MHD channel flow, these parameters will have directions as shown in Fig. 9. Note that the velocity will have only one component, u_x, and the B-field will be only in the z direction. It is assumed that the induced magnetic field is negligible compared to the applied field. Using the coordinate system of Fig. 9, the generalized Ohm's law given in Eq. (16) can be reduced to

$$j_x = \frac{\sigma}{1 + (\omega\tau)^2} \left\{ E_x - \omega\tau \left[E_y - uB \right] \right\} \tag{17}$$

and

$$j_y = \frac{\sigma}{1 + (\omega\tau)^2} \left\{ E_y - uB + \omega\tau \, E_x \right\} \tag{18}$$

where $\omega\tau = \dfrac{\sigma B}{n_e e}$ is the Hall parameter. It can be predicted that for accelerator conditions which would result in the desired simulation, the magnetic field, conductivity, and electron density will be such that $\omega\tau \leq 1.0$, compared to values of up to 10 in previous channels. This fact will have substantial bearing on the channel geometry.
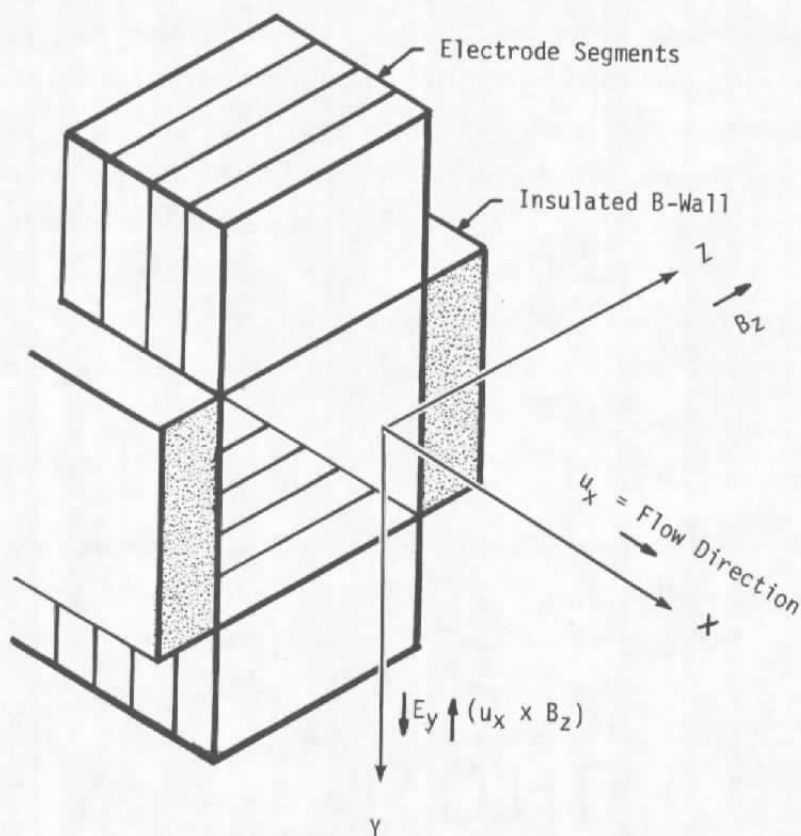
Figure 9. Coordinate system for MHD
channel flow.

Equations (17) and (18) then are the general expressions for the
current density in an ionized plasma flowing in the presence of electric
and magnetic fields. Note that the scalar conductivity is reduced by the
factor $1 + (\omega\tau)^2$.

The scalar conductivity can be considered to be a function of tem-
perature and pressure for a given seed concentration and is therefore a
calculable parameter. The conductivity will be discussed in more depth
in a later section.

4.2 DESCRIPTION OF ACCELERATOR CONFIGURATION

Discussions to this point have been of a general nature, and Eqs. (17)
and (18) were derived assuming no restrictions or limitations on any of the

23

parameters involved in their derivation. For the practical case, however, there are restrictions imposed by the configuration of the accelerator itself. For example, if the accelerator were composed of a continuous copper anode and a continuous copper cathode, it would be impossible to sustain an electric field in the x direction. E_x would then be zero in Eqs. (17) and (18) and the equations could be solved by specifying only one other electrical parameter. The various configurations impose various restrictions, of course, and the restrictions for each particular configuration will be discussed below.

4.2.1 Faraday Accelerator

The three most basic configurations of MHD accelerators are shown in Fig. 10. The segmented Faraday configuration consists essentially of a series of electrode pairs insulated from each other by the B-field walls and also insulated from the adjacent electrodes by high-grade insulation material. Note that each electrode pair requires its own individual power supply, and that the electrode pair, ionized plasma, and power supply comprise a closed circuit. The current must be conserved in this closed circuit and therefore no current can flow between adjacent electrode pairs. This means that no current is permitted to flow in the x direction (except for that allowed by finite electrode effect to be discussed later). For the Faraday case, then, Eqs. (17) and (18) become

$$j_x = 0 \tag{19}$$

and

$$j_y = \sigma(E_y - uB) \tag{20}$$

Since j_x does not produce any acceleration, but serves only to heat the gas, the Faraday channel is the most efficient of any configuration. It suffers from the fact that many independent power supplies are required, leading to a complicated power bank and wiring system. Because of its efficiency, however, much of the present study has centered around the Faraday case.
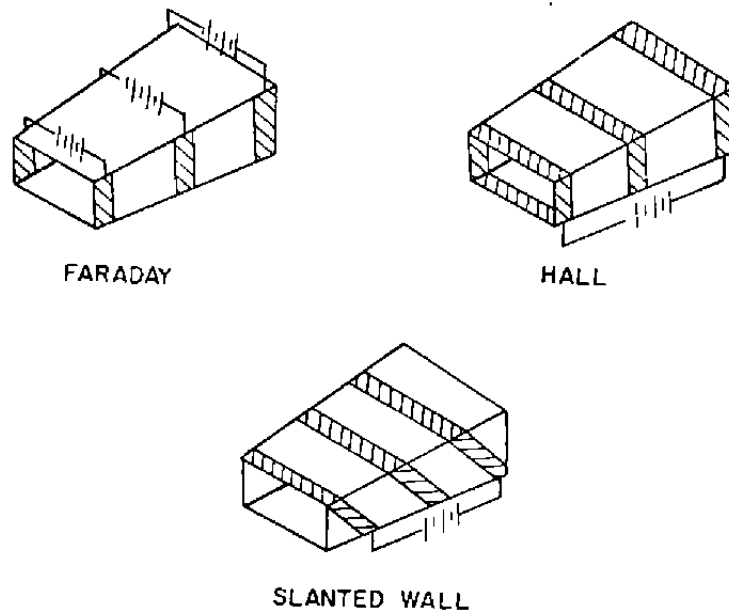
Figure 10. Modes of accelerator operation.

Since that is the case, one other point will be discussed. For the Hall component of the current to become identically zero requires infinitely fine electrode segmentation. In reality, it is not practical to have infinitely fine segmented electrodes and there will be an effective reduction in conductivity caused by finitely segmented electrodes. This reduction will be present in all modes of operation, even in the supposedly Hall-neutralized Faraday case. The finite length of the electrodes provides a return path for the Hall current produced by the Hall field. This allows a circulating current close to the electrode. When this circulating current is added to j_y, a current concentration is produced on opposite edges of the electrodes as shown in Fig. 11. As a first approximation, it is assumed that

$$j_x = j_{x_{ext}} - F j_y \qquad (21)$$

where F is a factor which depends on the electrode geometry. In Eq. (21) $j_{x_{ext}}$ is the current which flows in the external circuitry (including that

which would flow in the metal sidewalls of a slant-wall channel), and j_x is the actual current flow in the gas. With no Hall current in the external circuit (i.e., $j_{x_{ext}} = 0$), Eqs. (21) and (17) become

$$j_x = - F j_y = \frac{\sigma}{1 + (\omega\tau)^2} \left[E_x - \omega\tau(E_y - uB) \right] \qquad (22)$$
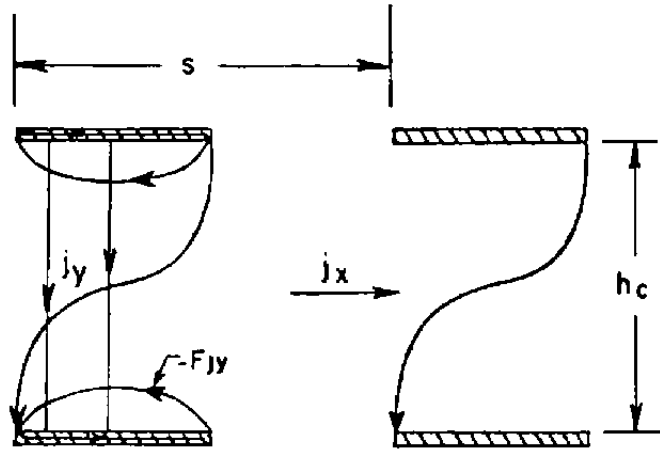
Figure 11. Geometry for finite electrode effect.

Solving for E_x and substituting into Eq. (18)

$$j_y = \frac{\sigma}{1 + \omega\tau \, F} \, (E_y - uB) \qquad (23)$$

In this case, the effective conductivity is reduced by $1 + \omega\tau \, F$.

The factor, F, used in Eq. (21) can be estimated by observation of Fig. 11. Note that for small insulator width-to-electrode width ratios, the current can be broken into two components of order s and h_c. As a first approximation, then, F can be defined as

$$F = \frac{s}{h_c} \qquad (24)$$

The degree of current concentration, then, is a function of the Hall parameter and the electrode spacing to channel height ratio. In general, the lower the Hall parameter the more efficient is the Faraday accelerator.

The direction of the applied electric field, induced electric field, current flow, and Lorentz force in a typical Faraday channel is shown in Fig. 12.
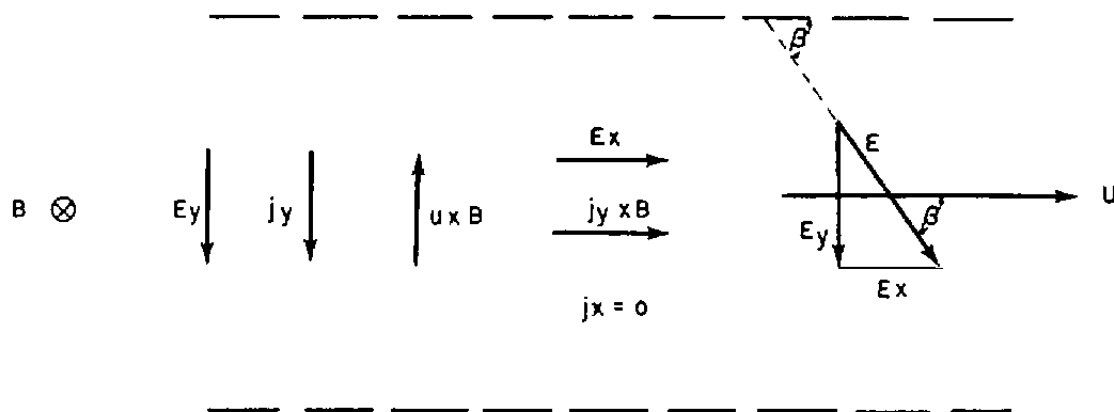
Figure 12. Direction of vector parameters
in Faraday accelerator.

4.2.2 Slant-Wall Accelerator

The basic principle for the slant-wall accelerator was derived from the Faraday accelerator. Consider the electric fields, E_x and E_y, in the Faraday channel (Fig. 12). If these fields are added vectorially, the resulting field is at some angle, ß, with the flow direction. A line drawn at right angles to this resultant field is an equipotential line, and hence, by definition, has no voltage gradient along the line. Since no voltage gradient exists to force current flow along the equipotential, it was reasoned that solid metal sidewalls could be placed along the equipotential lines and not affect the internal channel operation. Since the most efficient accelerator operation corresponds to the no Hall current condition (i.e., $j_x = 0$), it was reasoned that the slant-wall arrangement would maintain the advantage of low Hall current (as in the Faraday case) and also give the added advantage of two-terminal operation

27

as shown in Fig. 10. This means that the multitude of power supplies required to power each electrode pair in the Faraday channel may be replaced by one large power supply for a slant-wall accelerator. This is a distinct advantage; however, the overall efficiency is somewhat reduced since some Hall current does, indeed, flow in a slant-wall channel. This Hall current flow follows from the fact that, in a Faraday channel, E_y and E_x vary independently from each other. Then the ratio

can't elim.
Hall current

$$\phi = \frac{E_y}{E_x} \qquad (25)$$

varies from channel inlet to channel exit depending on how other channel parameters vary. For the slant-wall channel, however, this ratio is required to remain constant since it is not practical to build slant-wall channels with variable wall angle. This means that Faraday operation is not achieved. The Hall current flow may be in either the positive or negative direction and can even change directions inside the channel, depending on how closely the channel design conditions are matched.

Since the diagonal wall accelerator is a two-terminal device, with its attendant operational ease, it was considered during the present studies, but unfortunately, the device is not well suited to the present application. The slant-wall angle, shown in Fig. 13 with the direction of the other vector parameters, is a function of the Hall parameter. The channel is ideally suited to moderate values of the Hall parameter ($3 < \omega\tau < 5$) and becomes relatively inefficient at low Hall parameters produced at high static pressure levels. Furthermore, in channels where the Hall parameter varies significantly from inlet to exit, the wall angle would also have to vary to maintain low Hall currents. If it is assumed that the channel is constructed such at $j_x = 0$, Eq. (17) becomes

$$E_x = \omega\tau(E_y - uB) \qquad (26)$$

28

It can be seen from Fig. 13 that the angle which the solid sidewalls make with the flow direction is related to ϕ by the relation

$$\cot \theta = \phi = \frac{E_y}{E_x} \qquad (27)$$

Substituting E_x from Eq. (26)

$$\phi = \frac{1}{\omega\tau\left(1 - \dfrac{uB}{E_y}\right)} . \qquad (28)$$
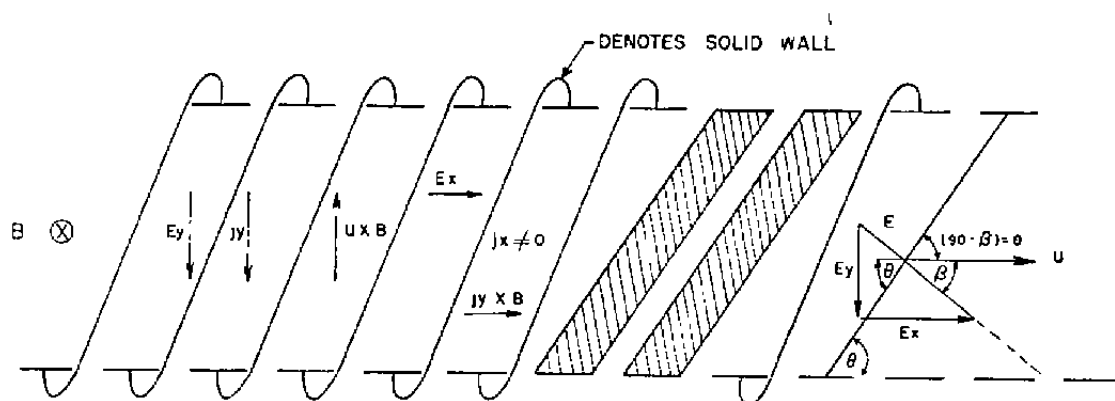
Figure 13. Direction of vector parameters
in slant-wall channel.

The term uB/E_y is a measure of accelerator efficiency, and it is desired that $uB/E_y \geq 0.7$. For that case, a low Hall parameter results in very low values of θ. To attain the high velocity and high-impact pressures in the present application, the channel must operate at high pressures, resulting in Hall parameters much less than one at the inlet. If $\omega\tau = 0.75$ is assumed in Eq. (28), then the resulting wall angle would be $\theta \approx 12$ deg. That, of course, would be an extremely difficult channel to fabricate. Futhermore, the Hall parameter increases significantly throughout the channel, and the wall angle would have to vary continuously to approach even reasonable efficiency. The slant wall channel was therefore eliminated as a possible configuration for a reentry facility accelerator.

4.2.3 Hall Accelerator

The Hall accelerator is inherently a two-terminal device and can be considered to be a limiting case of the slant-wall accelerator ($\phi = 0$). The general configuration of the Hall channel is shown in Fig. 10, and the direction of all vector parameters is shown in Fig. 14.

In the Hall device the voltage is applied in the axial direction. However, it is the transverse current which supplies the Lorentz force and this transverse current depends on the Hall parameter for its generation. This can be seen by noting that no electric field can be sustained in the y direction in a Hall accelerator ($E_y = 0$) and applying that fact to Eq. (18) gives

$$j_y = \frac{\sigma}{1 + (\omega\tau)^2} (\omega\tau\, E_x - uB) \qquad (29)$$

For high-velocity flow ($u \geq 3,000$ m/sec) and a B-field of 6 Tesla, $uB = 18,000$ v/m. If E_x is taken to be 4,000 v/m (approaching the value that can be sustained in an accelerator channel), the $\omega\tau$ must be greater than 4.5 for efficient operation. As previously noted, $\omega\tau$ is small (< 1) for the high-density conditions required to produce an impact pressure of 170 atm. The Hall accelerator, therefore, is not an attractive device for the present application.
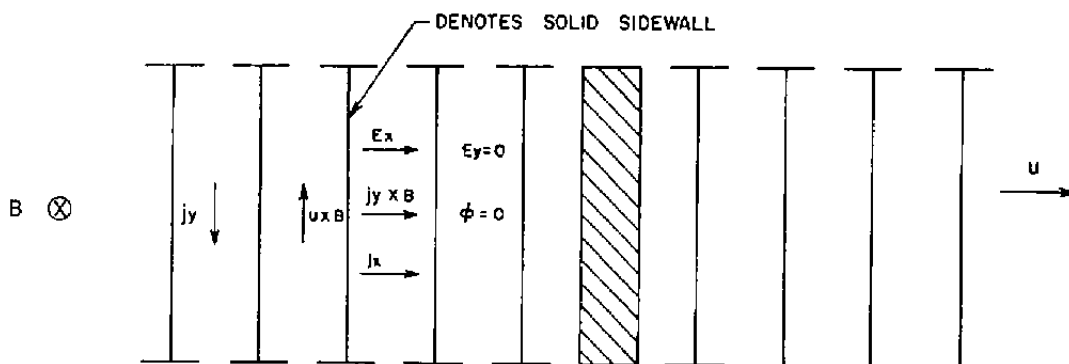
Figure 14. Direction of vector parameters in Hall accelerator.

4.2.4 Hybrid Accelerator

The term "hybrid" accelerator has not been previously defined in the literature. It is, in reality, a special version of the Faraday accelerator, or it might be considered to be a combination of a segmented Faraday and a continuous electrode Faraday. Instead of a finely segmented channel, requiring a multitude of power supplies, the hybrid channel is a very coarsely segmented channel requiring perhaps an order of magnitude fewer power supplies. The possibility of using such a channel was suggested by the results of some early studies. It was recognized that to achieve adequate electrical conductivity in the present high-pressure regime, the channel would have to be operated at somewhat higher temperatures. This fact can be seen from Fig. 15, where the conductivity is plotted as a function of temperature for constant pressures. Note that the conductivity has a strong pressure dependence, which in general is $\sigma \propto \frac{1}{\sqrt{p}}$. To maintain a high conductivity then, the temperature must be increased as the pressure is increased. This also results in a higher electron number density. Now it has been previously noted that

$$\omega\tau = \frac{\sigma B}{n_e e} \tag{30}$$

The Hall parameter therefore decreases rapidly as the pressure increases, caused by the increase in electron number density. Figure 16 shows the trend in the parameter as pressure and temperature are varied, assuming a unit magnetic field.

With the very low values of the Hall parameter obtained at high pressures, the tendency for the Hall current to flow is minimized, negating the necessity for fine segmentation. The performance degradation caused by the Hall current was noted in Eq. (23), repeated below

$$j_y = \frac{\sigma}{1 + \omega\tau\, F} (E_y - uB) \tag{23}$$
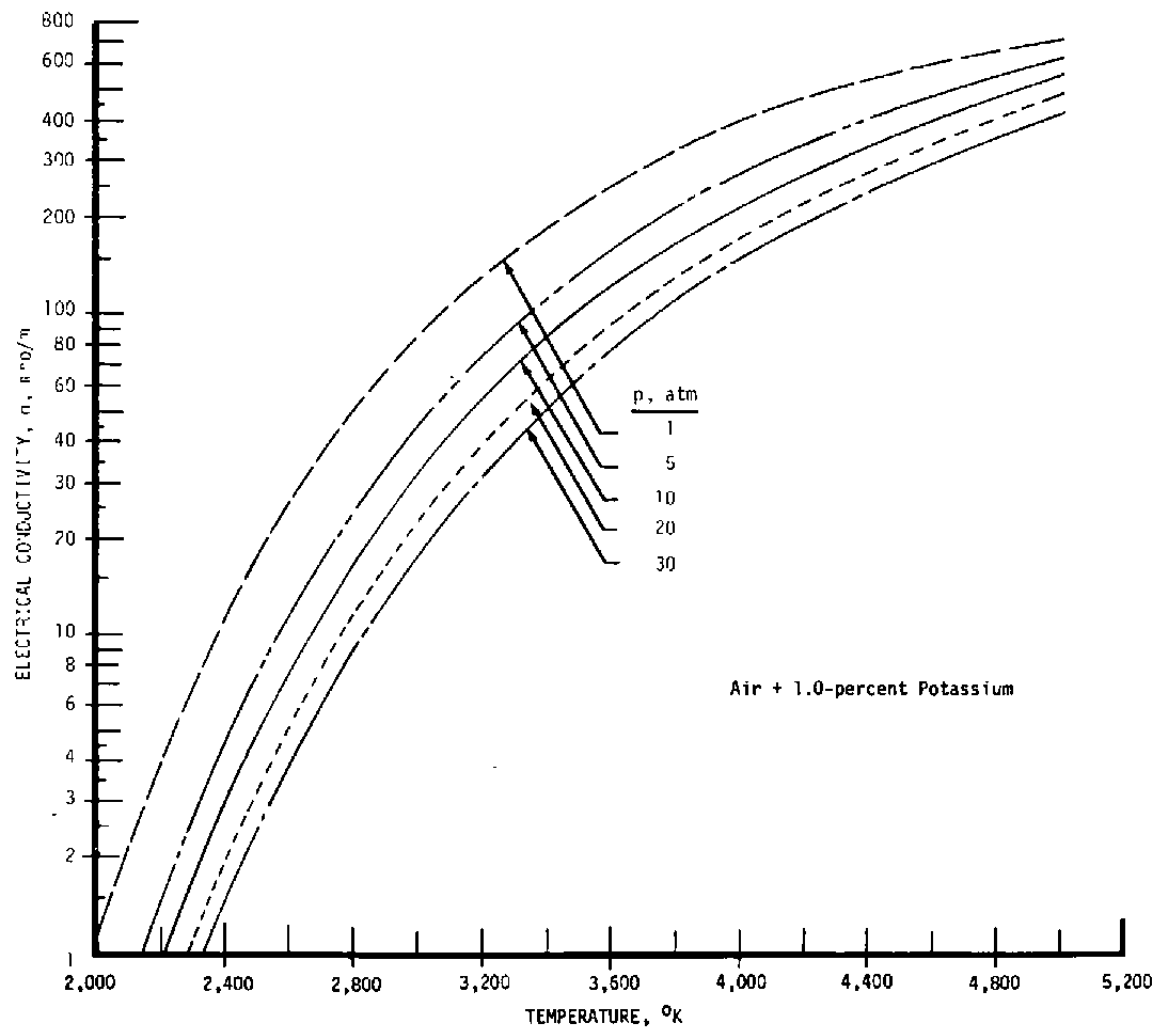
Figure 15. Electrical conductivity of
potassium-seeded air.
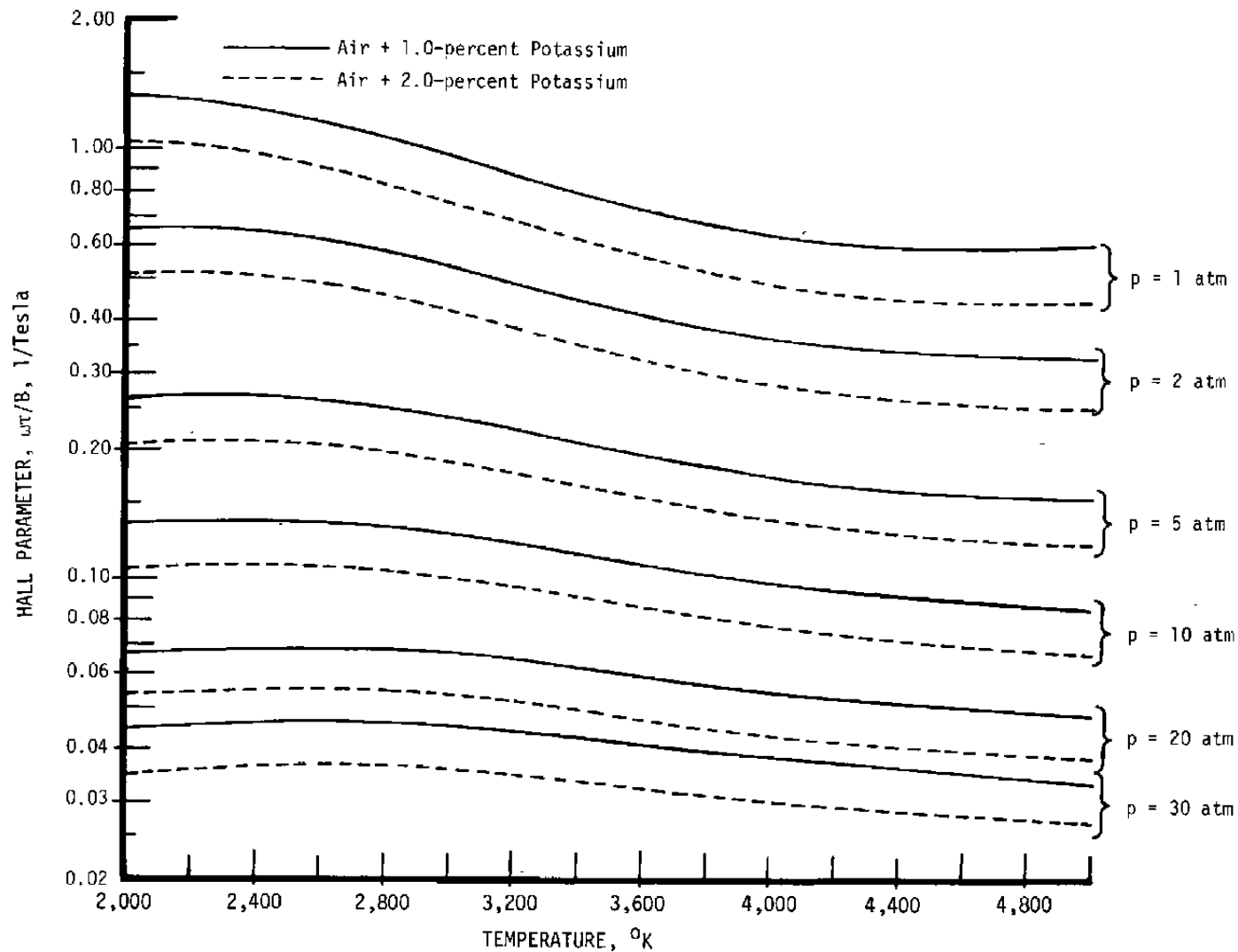
Figure 16. Hall parameter for potassium-seeded air.

The effective current flow which produces the accelerating force is reduced by the factor $1 + \omega\tau$ F, where F is a function of electrode geometry. Now, in a standard channel operating at low density, the Hall parameter might be as high as 10, and the factor F might be 0.1. In the high-pressure regime, where the Hall parameter is unity or less, the factor F could be increased by an order of magnitude with no more performance degradation than would occur in previously tested finely segmented Faraday channels.

It would not be practical, of course, to build a single continuous electrode channel since the electric field, E_y, would be equal to the applied voltage divided by the channel height and would be constant throughout the channel. The accelerating force would then increase the plasma velocity until the term uB in Eq. (23) approached the term E_y, thereby decreasing the current density and the accelerating force. In order to achieve a high exit velocity, a high, fairly uniform current density is required throughout the channel, requiring a tailored applied field. The electrodes in that case must be segmented at intervals and the applied field increased to maintain the required current density.

The accelerating flow results in a negative pressure gradient in the channel, of course, and the decreasing pressure results in increasing the Hall parameter, thereby increasing the tendency for the Hall current to flow. The practical channel, therefore, would probably be built with very coarse segmentation near the channel inlet, gradually increasing the fineness of the segmentation toward the channel exit.

4.3 PROTOTYPE ACCELERATORS

The earlier MHD accelerator research conducted at atmospheric pressure levels or below and at input power levels less than 1 MW cannot be expected to form an extrapolation base for the present application, where channel inlet pressures are above 20 atm and power levels on the order of 500 MW have been considered. The AEDC work was accomplished with segmented Faraday channels and the NASA-Langley effort was also on linear

34

accelerators. Some concern exists that diffuse current discharge cannot ①
be sustained at the higher pressure levels, and previous work gives no
insight to this problem. Also, the earlier work was accomplished at
magnetic field levels of 2 Tesla (T) or less; the present studies assume ②
three to five times that level. In light of these facts, the earlier
development efforts cannot be scaled directly to the present size. An
incremental development program would be required to extend the previous
experimental results into the present operating regime.

5.0 DESCRIPTION OF COMPUTER PROGRAMS

5.1 GENERALIZED ONE-DIMENSIONAL MHD CHANNEL FLOW

The governing equations for generalized MHD channel flow, including
friction and heat transfer, are given by:

Momentum
$$\rho u \frac{du}{dx} + \frac{dp}{dx} = j_y B - \frac{4 \tau_w}{D_h} \qquad (31)$$

Energy
$$\rho u \frac{dH}{dx} = j_x E_x + j_y E_y - \frac{dq}{dx} \qquad (32)$$

Continuity
$$\rho u A = \dot{m} \qquad (33)$$

In addition, the equation of state is also considered to be a govern-
ing equation. However, in lieu of the perfect gas equation of state, the
real gas tables of Hilsenrath and Klein (Ref. 6) are used to obtain the
thermodynamic properties and equilibrium composition. The equations above
assume that one-dimensional flow exists and that such a one-dimensional
analysis is valid as a first approximation. The assumption that the flow
is one-dimensional means that all variables are assumed to vary only with
x, the distance down the channel. It is further assumed that the flow
velocity, applied magnetic field, and applied electric field are mutually

$$\frac{dH}{dx} = RT \frac{d^{S}/_R}{dx}$$

$$\rho u \frac{d'H}{dy} = \vec{J} \cdot \vec{B}$$

$$\frac{dH}{d^{S}/_R} = RT$$

$$\rho u \, RT \frac{d^{S}/_R}{dx} = \vec{J} \cdot \vec{B}$$

35

perpendicular at any point in the channel as shown in Fig. 9. It is also assumed that two-dimensional effects, such as finite electrode effects already discussed, skin-friction, and heat-transfer losses may be considered separately, but still in the one-dimensional framework.

5.1.1 Basic Program Structure

Equations (31), (32), and (33) can be reduced to two independent differential equations using the distance down the channel, x, as the independent variable. Entropy and pressure were chosen as the dependent parameters since they are convenient properties to use in the derivation and also because they are convenient properties with which to enter the real gas tables. Using

$$H = h + \frac{u^2}{2} \tag{34}$$

Equation (32) becomes

$$\rho u^2 \frac{du}{dx} + \rho u \frac{dh}{dx} = j_x E_x + j_y E_y - \frac{dq}{dx} \tag{35}$$

Multiplying u times the momentum equation and subtracting from Eq. (35) yields

$$\rho u \frac{dh}{dx} - u \frac{dp}{dx} = j_x E_x + j_y (E_y - uB) - \frac{dq}{dx} + u\Sigma \tag{36}$$

where

$$\Sigma = \frac{4 \tau_w}{D_h} \tag{37}$$

From the Second Law of Thermodynamics

$$TdS = dU + pdv \tag{38}$$

Now

$$dh = d(U + pv) = dU + pdv + vdp \tag{39}$$

36

Then

$$dU = dh - vdp - pdv \tag{40}$$

Substituting Eq. (40) into Eq. (38)

$$TdS = dh - vdp - pdv + pdv \tag{41}$$

or

$$TdS = dh - \frac{dp}{\rho} \tag{42}$$

Multiplying Eq. (42) by ρu and considering differentiation with respect to x gives

$$\rho uT \frac{dS}{dx} = \rho u \frac{dh}{dx} - u \frac{dp}{dx} \tag{43}$$

Equation (43) can be written as

$$\rho u \, RT \frac{d \frac{S}{R}}{dx} = \rho u \frac{dh}{dx} - u \frac{dp}{dx} \tag{44}$$

Now the right-hand side of Eq. (44) is identical to the left side of Eq. (36), then

$$\rho u \, RT \frac{d \frac{S}{R}}{dx} = j_x E_x + j_y(E_y - uB) - \frac{dq}{dx} + u\Sigma \tag{45}$$

Solving for $\dfrac{d \frac{S}{R}}{dx}$ gives

$$\frac{d \frac{S}{R}}{dx} = \frac{1}{\rho u \, RT} \left[j_x E_x + j_y(E_y - uB) - \frac{dq}{dx} + u\Sigma \right] \tag{46}$$

The equation for dp/dx is not so simple but is quite straightforward. From Eq. (33)

$$\frac{1}{\rho}\frac{d\rho}{dx} + \frac{1}{u}\frac{du}{dx} + \frac{1}{A}\frac{dA}{dx} = 0 \qquad (47)$$

Equation (47) can be written as

$$\frac{1}{\rho}\left(\frac{\partial\rho}{\partial\frac{S}{R}}\right)_p \frac{d\frac{S}{R}}{dx} + \frac{1}{\rho}\left(\frac{\partial\rho}{\partial p}\right)_{S/R} \frac{dp}{dx} + \frac{1}{u}\frac{du}{dx} + \frac{1}{A}\frac{dA}{dx} = 0 \qquad (48)$$

From Eq. (31)

$$\frac{du}{dx} = \frac{j_y B - \dfrac{dp}{dx} - \Sigma}{\rho u} \qquad (49)$$

Substituting Eq. (49) into Eq. (48), using d S/R/dx from Eq. (46), and rearranging, Eq. (48) becomes

$$-\left(\frac{\partial \ln \rho}{\partial p}\right)_{S/R} \frac{dp}{dx} + \frac{1}{\rho u^2}\frac{dp}{dx}$$

$$= \frac{\left(\dfrac{\partial \ln \rho}{\partial \frac{S}{R}}\right)_p}{\rho u\ RT}\left[j_x E_x + j_y(E_y - uB) - \frac{dq}{dx} + u\Sigma\right] + \frac{j_y B}{\rho u^2} + \frac{1}{A}\frac{dA}{dx} - \frac{\Sigma}{\rho u^2} \qquad (50)$$

Solving for $\dfrac{d \ln p}{dx}$

$$\frac{d \ln p}{dx} = \frac{\dfrac{1}{\rho u\ RT}\left(\dfrac{\partial \ln \rho}{\partial S/R}\right)_p \left[j_x E_x + j_y(E_y - uB) - \dfrac{dq}{dx} + u\Sigma\right]}{\dfrac{p}{\rho u^2} - \left(\dfrac{\partial \ln \rho}{\partial \ln p}\right)_{S/R}}$$

$$+ \frac{1}{A}\frac{dA}{dx} + \frac{j_y B}{\rho u^2} - \frac{\Sigma}{\rho u^2} \Bigg/ \frac{p}{\rho u^2} - \left(\frac{\partial \ln \rho}{\partial \ln p}\right)_{S/R} \qquad (51)$$

Converting to common base logarithms, because Mollier diagram tables are calculated for S/R and log P, gives

$$\frac{d \log p}{dx} = \frac{\frac{1}{\rho u \, RT} \left(\frac{\partial \log \rho}{\partial \, S/R}\right)_p \left[j_x E_x + j_y(E_y - uB) - \frac{dq}{dx} + u\Sigma\right]}{\frac{p}{\rho u^2} - \left(\frac{\partial \log \rho}{\partial \log p}\right)_{S/R}}$$

$$+ \left.\frac{1}{2.303A}\frac{dA}{dx} + \frac{j_y B - \Sigma}{2.303 \, \rho u^2}\right/ \frac{p}{\rho u^2} - \left(\frac{\partial \log \rho}{\partial \log p}\right)_{S/R} \tag{52}$$

Using Eqs. (46) and (52) allows integration down the channel in terms of channel parameters. The denominator of Eq. (52) can be transformed into the expression $-\frac{p}{\rho u^2}\left[M^2 - 1\right]$ by using $a^2 = \left(\frac{\partial p}{\partial \rho}\right)_S$. Because of the term $\left[M^2 - 1\right]$ the program fails at sonic conditions.

Equations (46) and (52) are the basic equations for integration down a given accelerator channel, and form the basis for the "main program." Other parameters are computed in specialized subroutines.

5.1.2 Channel Configurations

With a given set of inlet conditions, including pressure and entropy, all remaining parameters required in the integration of the two independent equations are calculated in subroutines. The geometry is specified in the area subroutine, the field strength and profile are specified in the B-field subroutine, and thermodynamic properties are called from the real gas tables. The specification of a particular accelerator configuration is accomplished with various configuration subroutines. For each instance, the restrictions of a particular configuration are applied to Eqs. (17) and (18) and the resulting equations are programmed to define that particular option. A total of fourteen configuration subroutines allow analysis of any linear channel configuration.

5.1.3 Electrical Conductivity Subroutines

The conductivity subroutine calculates the electron number density, scalar conductivity, and Hall parameter with pressure, temperature, seed concentration, and seed ionization potential as inputs. The derivation of the conductivity equations is much too complex to present here; only a brief discussion will be included.

The conductivity calculations assume that all free electrons are furnished by the seed material, that the seed is singly ionized, that equilibrium ionization exists, and that the ionization reaction is governed by the Saha equation (Refs. 7 and 8). As it turns out, those assumptions are quite valid and introduce negligible error. Rigorous derivations exist for the conductivity of a slightly ionized plasma (Ref. 9) and for the case of a fully ionized plasma (Ref. 10), and the conductivity is calculated using those methods and the collision cross-section data of Shkarofsky, Bachynski, and Johnston (Ref. 11). Although no rigorous derivation exists for a gas with an arbitrary degree of ionization, the method used here is that proposed by Lin, Resler, and Kantrowitz (Ref. 12). They postulate that the resistance caused by neutral particles and ions should be additive, i.e.,

$$\frac{1}{\sigma} = \frac{1}{\sigma_{en}} + \frac{1}{\sigma_{ei}} \tag{53}$$

The conductivity calculated by Eq. (53) is rigorously correct at each ionization limit (weakly ionized, fully ionized), but some error is introduced for the partially ionized case. Demetriades and Argyropoulos (Ref. 13) have developed other expressions for the conductivity and their methods have been used to compute corrective coefficients to Eq. (53).

5.1.4 Heat-Transfer Subroutines

Heat-transfer calculations are performed using Reynolds' analogy with a turbulent flow friction factor, modified to include the effect of electrical discharge. Though this procedure is not exact, it is felt that

the heat losses are calculated with sufficient accuracy that the accelerator performance calculations are correct to a first approximation. The option is included to specify a heat-transfer-rate profile down the channel if it is desired to calculate heat loads by some other method and use those as input quantities.

The heat loads experienced by an accelerator channel operating in the severe environment required to produce the desired reentry simulation are extremely high (10 kw/cm^2). Such high heat-transfer rates are approaching the upper limit for cooling of copper walls. Heat loads of 14 kw/cm^2 have been cooled in arc heater chambers, but it is recognized that judicious and intricate design will be required to cool the electrode walls.

An even more severe problem exists with the insulator walls. Not only must they sustain the high heat loads, but they must also maintain their integrity as electrical insulators. Most insulators, of course, have low thermal conductivity making backside cooling essentially impossible at the expected heat-transfer rates. In addition, the insulator walls will be subjected to high thermal shock. Grave concern exists over the ability of any existing insulator material to withstand the severe environment. For this reason, a study was conducted to ascertain the feasibility of film cooling the insulator walls. The description of the computer program used in that study is discussed in Section 5.2.

5.2 TWO-DIMENSIONAL CHANNEL FILM COOLING ANALYSIS

The difficulties anticipated in cooling the insulating walls of the MHD accelerator by using conventional cooling techniques suggest cooling the insulator walls with a film of cold air. A complete viscous film cooling analysis of two opposing walls of a rectangular channel requires a three-dimensional approach. As a suitable three-dimensional program was not available for this study, an existing two-dimensional program was modified to approximate some of the three-dimensional effects. The first attempts at this analysis assumed that the two-dimensional channel could

be approximated by an axisymmetric duct of the same hydraulic radius.
This would be a reasonable approximation for a thin cooling film; how-
ever, the resulting analysis indicated that a thick cooling film was
required. The present analysis described below models the channel length,
width, and height; however, the no-slip boundary condition is imposed only
on the insulated walls and not at the electrode walls, reducing the
problem to a special case of the general two-dimensional problem. The
results of this analysis will be slightly optimistic since the momentum
and energy losses through the electrode walls are neglected. The use of
this admittedly optimistic model is warranted in view of the preliminary
nature of the study.

5.2.1 Computer Code Description

The basic program is a version of the much-used Spaulding-Patankar
turbulent boundary-layer program (Ref. 14) as modified by Kessel (Ref.
15) to calculate the flow in slender channels of specific geometry for
a given reservoir total pressure and total enthalpy. The equations
solved are:

Continuity

$$\frac{\partial}{\partial x} (\rho u) + \frac{\partial}{\partial z} (\rho v) = 0 \tag{54}$$

Momentum

$$\rho u \frac{\partial u}{\partial x} + \rho v \frac{\partial u}{\partial z} = - \frac{dp}{dx} + j_y B_z + \frac{\partial}{\partial z} \left[\frac{\partial u}{\partial z} + \overline{\rho u' v'} \right] \tag{55}$$

Stagnation Enthalpy

$$\rho u \frac{\partial H}{\partial x} + \rho v \frac{\partial H}{\partial z} = \frac{\partial}{\partial z} \left[\frac{\mu_{eff}}{Pr_{eff}} \frac{\partial H}{\partial z} + \mu_{eff} (1 - \frac{1}{Pr_{eff}}) \frac{\partial}{\partial z} (\frac{u^2}{2}) \right] + j_y E_y \tag{56}$$

The $j_x B_x$ term in the x momentum equation and the $j_y E_y$ term in the energy
equation are the only modifications necessary to the governing equations

to calculate the first-order MHD effects in the channel flow field. The MHD terms which have been neglected limit the applicability of these equations to cases in which there is zero current in the x direction and in which the normal pressure gradient is low.

The transform variables

$$\xi = x \tag{57}$$

$$\rho u = \frac{\partial \psi}{\partial z} \tag{58}$$

$$-\rho v = \frac{\partial \psi}{\partial x} \tag{59}$$

$$\omega = \frac{\psi - \psi_i}{\psi_e - \psi_i} \tag{60}$$

are used to eliminate the continuity equation and transform the x-momentum and energy equations into the general form

$$\frac{\partial \phi}{\partial \xi} + (a + b\omega)\frac{\partial \phi}{\partial \omega} = \frac{\partial}{\partial \omega}\left(c\frac{\partial \phi}{\partial \omega}\right) + d \tag{61}$$

Tabular values of P_r and d are given in Table 2. The primary dependent variables of these two equations are u, p, and h. The equation of state:

$$\rho = \frac{p}{h}\frac{1}{\left[RZ\frac{T}{h}\right]} \tag{62}$$

which is formulated in terms of p and h completes the set of equations to be solved. The compressibility correction factor $(RZ\frac{T}{h})$ is tabulated in terms of p and h. It should be noted that this approach is valid for any equilibrium real gas whose properties can be tabulated as a function of p and h.

Table 2. Program Variables in the Patankar-Spaulding Method (Ref. 13)

Dependent Variable ϕ	P_r	$P_{r_{eff}}$	Source Term, d
u	-	-	$-\dfrac{1}{\rho u}\dfrac{dp}{dx} + \dfrac{j_y B_z}{\rho u}$
H	0.7	0.9	$\dfrac{\partial}{\partial\omega}\left[\dfrac{\rho u\,\mu_{eff}}{(\psi_e - \psi_I)^2}\left\{\left(1 - \dfrac{1}{P_{r_{eff}}}\right)\right\}\dfrac{\partial\frac{u^2}{2}}{\partial\omega}\right] + \dfrac{j_y E_y}{\rho u}$

The effective turbulent viscosity in the above equations is calculated using the mixing length model:

$$\mu_{eff} = \rho\ell^2\left|\frac{\partial u}{\partial r}\right| \qquad (63)$$

where

$$\ell = kr \qquad 0 < r \le \frac{\lambda r_\ell}{k}$$

$$\ell = kr_\ell \qquad \frac{\lambda r_\ell}{k} < Z \qquad (64)$$

The expression for effective viscosity is modified near the wall using the Van Driest expression as modified by Patankar:

$$\mu_{eff} = \mu + \rho k^2 r^2\left[1 - \exp\frac{-r\sqrt{\tau_w\rho}}{\mu A^+}\right]^2\left|\frac{\partial u}{\partial r}\right| \qquad (65)$$

The Van Driest hypothesis damps out the turbulent contribution to the effective viscosity near the wall so that the effective viscosity equals the molecular viscosity at the wall. This expression does not appear explicitly in the computer program but is implicit in the formulation of the special wall functions that Patankar derived. No modifications have been made to these wall functions to correct for any MHD effects, the assumption being that the large viscous forces at the wall will be much larger than these MHD body forces.

The wall boundary conditions are

$$u = 0 \tag{66}$$

$$H = h_{wall} \tag{67}$$

$$\frac{\partial p}{\partial r} = 0 \tag{68}$$

The parameter h_{wall} may either be calculated using the upstream wall heat flux and the wall thermal properties, set to a predetermined value, or set to produce zero heat transfer (adiabatic wall).

The centerline boundary conditions are calculated using the centerline symmetry condition for fully merged viscous flow for the velocity and the enthalpy.

The distribution of pressure versus length must be specified or calculated to satisfy the sonic flow condition at the nozzle throat:

$$D = D* \tag{69}$$

$$\frac{\partial D}{\partial x} = 0 \tag{70}$$

The inlet static conditions are varied iteratively to achieve flow matching at the throat. Downstream of the throat the static pressure may be specified to produce the desired nozzle radius according to

$$dp = \rho u^2 \frac{1}{1 - M^2} \frac{dA}{A} \tag{71}$$

45

A more detailed description of the unmodified program may be found in Refs. 14 and 15.

The momentum and energy equation contains terms B_z, J_y, and E_y. In a complete treatment of the problem these terms would be part of the solution. A much simpler alternative is used here. The centerline current, J_y, and magnet field strength, B_z, are specified as input data as a function of channel length. The conductivity σ is determined from curve fits to conductivity data calculated as a function of pressure and enthalpy according to the methods described in Section 5.1 above. The centerline electric field strength E_y is calculated from Ohm's law:

$$E_y = \frac{j_y}{\sigma_{\phi}} + u_{\phi} \, B_z \qquad (72)$$

and is assumed to vary only as a function of channel length. The variation in current is then computed as a function of channel width using Ohm's law and the value of σ determined from the gas properties which also vary as a function of channel width. The electrical power dissipated in the gas is also calculated and integrated to determine the total electrical power required.

5.2.2 Special Geometry Approximation

The assumed MHD accelerator channel geometry is shown in Fig. 17. The ionized gas enters the channel from an axisymmetric supersonic nozzle which is mounted on an arc heater. The flow through the nozzle is calculated using the water-cooled copper wall option in the basic program. At the beginning of the accelerator channel, the flow is assumed to undergo transition perfectly from the axisymmetric to the two-dimensional channel of specified aspect ratio with no loss or gain in mass, momentum, or energy. The channel aspect ratio, an input specified value, is the ratio of channel height to width (see Fig. 17). The channel flow area is recomputed after each step in accordance with the prescribed boundary conditions, and the channel width is adjusted to produce the desired aspect ratio. Effectively, the aspect ratio controls the width of the channel.
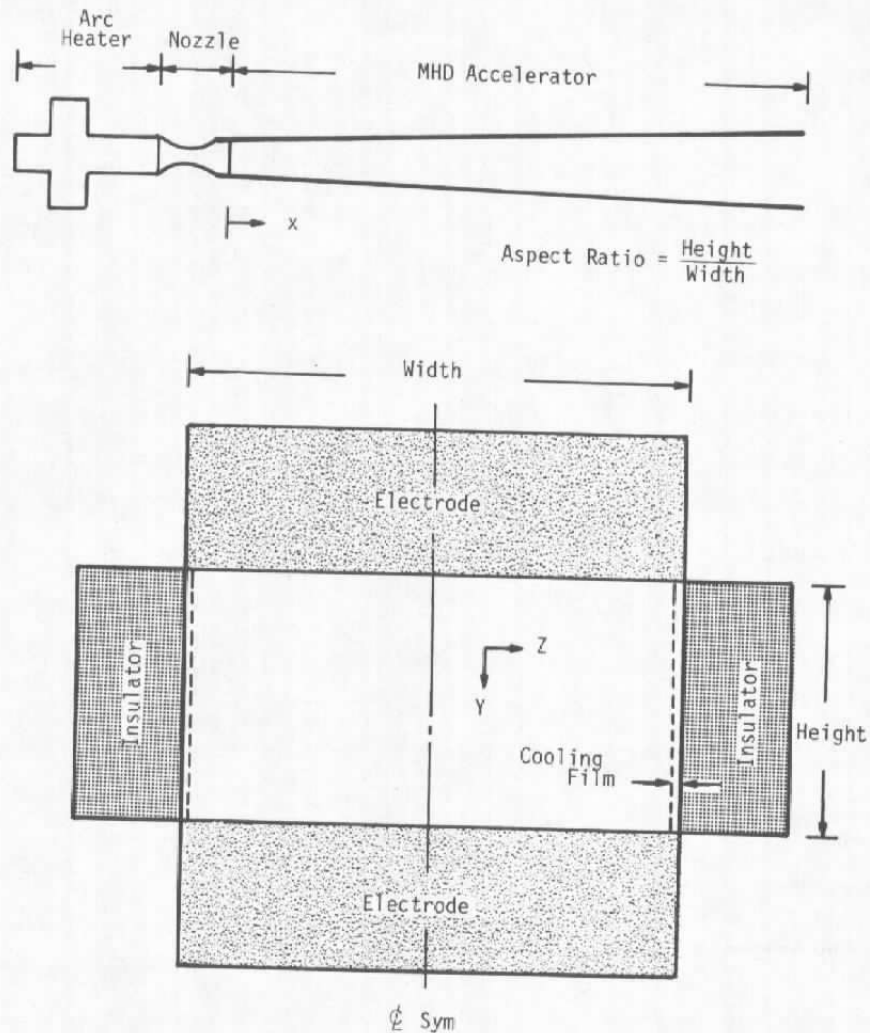
Figure 17. Assumed channel geometry for
film cooling study.

Calculations for a low aspect ratio are unrealistically optimistic since
the electrode wall losses, which are ignored, are roughly inversely pro-
portional to the aspect ratio. On the other hand, calculations for a high
aspect ratio are realistic but uninteresting since a high aspect ratio
results in high insulator wall friction and heat-transfer losses. An
optimum aspect ratio exists but cannot be accurately estimated unless a
proper accounting of the electrode wall losses is included in the analysis.

5.2.3 Computer Code Checkout

The basic program has been modified to stop the calculation at any point and add a cooling film of specified total pressure, enthalpy, and thickness. An option allows the film cooling restart to be initiated when the wall temperature reaches a specified value. This film cooling option is highly idealized. The cooling flow is assumed to be injected without distortion and to be parallel to the wall. Every real injection orifice would have finite edge dimensions and would induce additional mixing. The MHD accelerator pressure distribution is calculated for an axisymmetric case, and this pressure distribution is used in the film-cooled accelerator calculation; hence, the program calculates the contour of a film-cooled MHD accelerator necessary to produce the same static pressure gradient as the input accelerator geometry would produce.

The film-cooling option was checked by computing the performance of the film-cooled axisymmetric nozzle shown in Fig. 18 whose thermal performance data are given in Ref. 16.
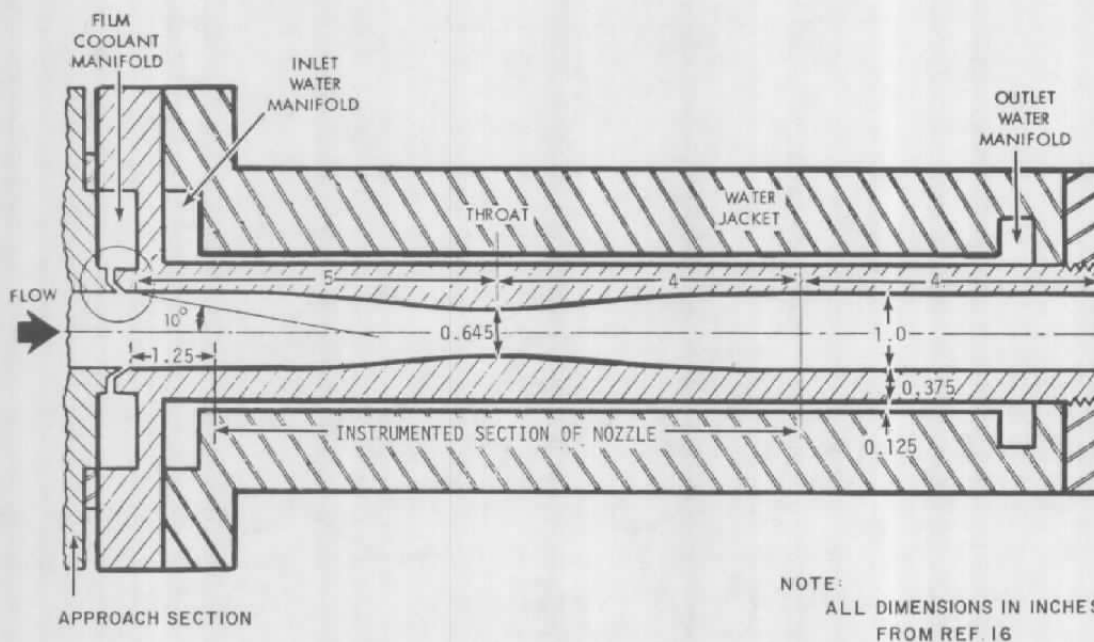
Figure 18. Film-cooled nozzle configuration.

The film-cooling computer code was used to predict the performance
of the nozzle for three test conditions. A comparison of the predicted
and measured wall temperature is shown in Fig. 19. The program is seen
to overpredict the nozzle wall temperature in the vicinity of the throat.
This small error, which is $25^\circ R$ or about 3.8 percent of the wall tempera-
ture or 25 percent of the wall temperature rise above cooling water
temperature, is not surprising in view of the fact that the thick nozzle
wall liner permits large axial heat flows which cannot be accounted for
in the parabolic (i.e., marching) slender channel computer code. The
agreement between the calculations and the test data is much better in
the region away from the throat. Another probable cause for the throat
discrepancy is that the turbulence model is inadequate in the region of
high axial pressure gradients. The shortcomings in this method of analy-
sis are not serious, since this application of the film cooling modifica-
tion deals mainly with the thermal behavior in the accelerator channel
where the axial pressure gradients are low and where the insulated
channel wall will limit axial heat conduction.
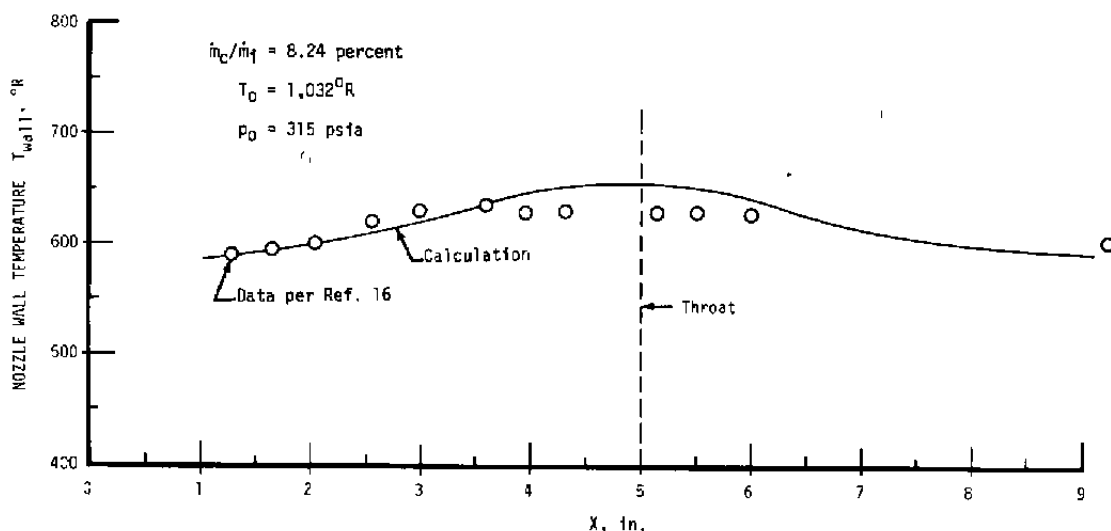
Figure 19. Comparison of measured and predicted film-
cooled nozzle wall temperature as a function
of length.

6.0 RESULTS OF ANALYTICAL STUDIES

6.1 POWER CONSIDERATIONS

As noted in Section 3.0, the production of high-enthalpy, high-velocity, and high-density gas streams requires enormous amounts of electrical energy. The power levels required can be seen by referring to Table 1, where the desired test model diameters are listed, and Fig. 7, where the power required to produce a given diameter flow is shown in graphic form. The gas stream power is shown to be on the order of 50 MW for the minimum desired nosetip size, and ranges up to something in excess of 10,000 MW for full-scale nose cones. The maximum required power level is clearly in excess of the installed capacity of any existing test installation. From the practical standpoint, then, the present study was limited to accelerator systems whose power requirement fell in the general range of existing power capability, or to a level which could reasonably be expected to exist within the next decade. Table 3 shows the presently installed capacity at AEDC, as well as the projected capacity in 1982. It might be pointed out that development of any accelerator facility would probably extend into that time period.

If a 50-percent efficient energy addition system is assumed, about 100-MW electrical energy would be required to produce the 50 MW in the gas stream shown as a minimum desired in Fig. 7. That power level agrees quite nicely with the 120-MW maximum step change currently existing. For that reason, a great deal of the present study has centered around that power level. In particular, extensive calculations have been performed on accelerator channels with a nominal 50-MW electrical input. An accelerator channel of this size would use the existing 40-MW segmented arc heater of the AEDC High Enthalpy Arc Tunnel (HEAT) as the plasma generator.

MHD-augmented arc systems with a much higher power level were also considered, of course, and the results of those studies will also be discussed. In general, the power levels were limited to the maximum noted in Table 3.

Table 3. Present and Projected Power Capacity at AEDC

Total Continuous Capacity of Lines Feeding AEDC: 900 MVA

(without Overheating Conductors)

Present Contract with TVA:

Maximum Daytime Power:	225 MW
Maximum Nighttime Power:	350 MW
Maximum Rate of Change:	60 MW/min
Maximum Step Change:	60 MW
Maximum Step Change: (with Prior Notice)	120 MW

Circa 1982 Power Capacity

161-KV Transmission Line — Existing	
320-KV Transmission Line — 1980	
820-KV Transmission Line — 1982	
Maximum Step Change	500 MW (765 MVA at 0.7 PF)
Maximum Step Change (Special Operational Procedures)	700 MW (1,000 MVA at 0.7 PF)

6.2 HIGH FIELD STRENGTH MAGNETS

An indication of the degree of accelerating force in an accelerator channel is given by the interaction parameter, $\left(\sigma B^2 L/\rho u,\right)$ where L is the channel length. In the present application, high velocity and high density are required, both tending to decrease the interaction parameters. Furthermore, the minimum possible channel length is desired to minimize viscous losses. For those reasons, and since the interaction parameter is proportional to B^2, the highest achievable magnetic field strength is desired. In order to generate realistic accelerator performance data, however, the assumed field strengths must be limited to

51

that which can reasonably be expected in the foreseeable future. The present studies assumed field strengths from 6 T to 10 T with the majority of calculations being performed at the 8-T level.

The values above were based on the projected magnet technology within the next decade. It can generally be stated that the upper limit for continuous duty, water-cooled magnets is on the order of 6 T. High current densities are required to produce field strengths of this level, and the resistivity of copper at room temperature or above is such that careful cooling design is required to dissipate the high power load. AEDC is constructing two large magnets capable of continuous operation, one for 4 T and the other to 4.5 T. Increased magnet technology will, no doubt, extend that performance.

Recent interest in MHD power generation has led to the initiation of numerous magnet research and development efforts. As in the case with MHD accelerators, high field strengths are desired. Since superconducting magnet technology is currently lagging the requirement, interest has been generated in cryogenically cooled magnets operated in the pulsed mode. Magnets of this type have been fabricated to allow basic research in MHD generators to generate a data base for design of longer duration facilities. Based on the present technology level, cryogenically cooled, pulsed magnets can be fabricated which will generate 8 T for 15-sec duration, adequate to meet test time requirements for reentry vehicles. ← Table 1

Extensive research and development will be required to produce a 10-T magnet; however, such development is not unrealistic. Again, commercial MHD power generation has provided the impetus needed to significantly advance the magnet technology, especially superconducting technology. The Francis Bitter National Magnet Lab (FBNML) has performed a reasonably detailed preliminary design for a 7-T superconducting magnet of a size commensurate with that required for MHD accelerators (Ref. 17). The FBNML is also involved in a joint effort intended to culminate in a magnet suitable for baseload MHD generators within ten years (Ref. 18).

Conceptual designs are shown in that report showing peak fields of 8.9 T for magnets five times the size required for the largest accelerator facility considered. Based on active development programs, then, a 10-T superconducting magnet of the required size is considered possible within the next decade.

6.3 ACCELERATOR PERFORMANCE CALCULATIONS

With the power level range and magnet field strengths dictated by practical considerations, a matrix of accelerator performance calculations was generated using the previously described computer program. The matrix was computed over a wide arc heater performance envelope for various seed rates, current densities, and channel expansion ratios. The channel inlet conditions, like the power levels and field strengths, were limited to values which can be produced by existing arc heaters or arc heaters which normal development should produce in the next decade.

The first series of computer solutions was aimed at determining the increase in test performance capability which could be obtained by adding an MHD accelerator to the present HEAT Facility. The assumed power level was a nominal 50-MW electrical power input, with channel inlet conditions commensurate with the performance envelope of the HEAT segmented arc. Figure 20 shows the parameter variation down the channel for a typical run, as well as the exit conditions. The desired Mach number, impact pressure, and enthalpy are shown as solid symbols at the accelerator exit. It can be seen that the enthalpy is closely duplicated, but both impact pressure and Mach number are well below the desired level. This leads to a general conclusion on those parameters. If the desired velocity is achieved, then $u^2/2$ is equivalent to the desired enthalpy. However, the accelerator flow stream must have sufficient static enthalpy to maintain adequate ionization of the seed material. This means that the total enthalpy will always be too high when the desired Mach number is achieved, and those parameters cannot be uncoupled in an MHD accelerator.

53

Though the performance shown in <u>Fig. 20</u> is well below that desired, it is equivalent to isentropic expansion from a 1,350-atm reservoir, a <u>significant increase</u> over <u>present test capability</u>. In Table 4, performance of this MHD-augmented HEAT Facility is compared with the minimum acceptable simulation of Table 1. The performance is clearly deficient. Hypersonic pressure distributions are not duplicated, nor is the proper shear level.
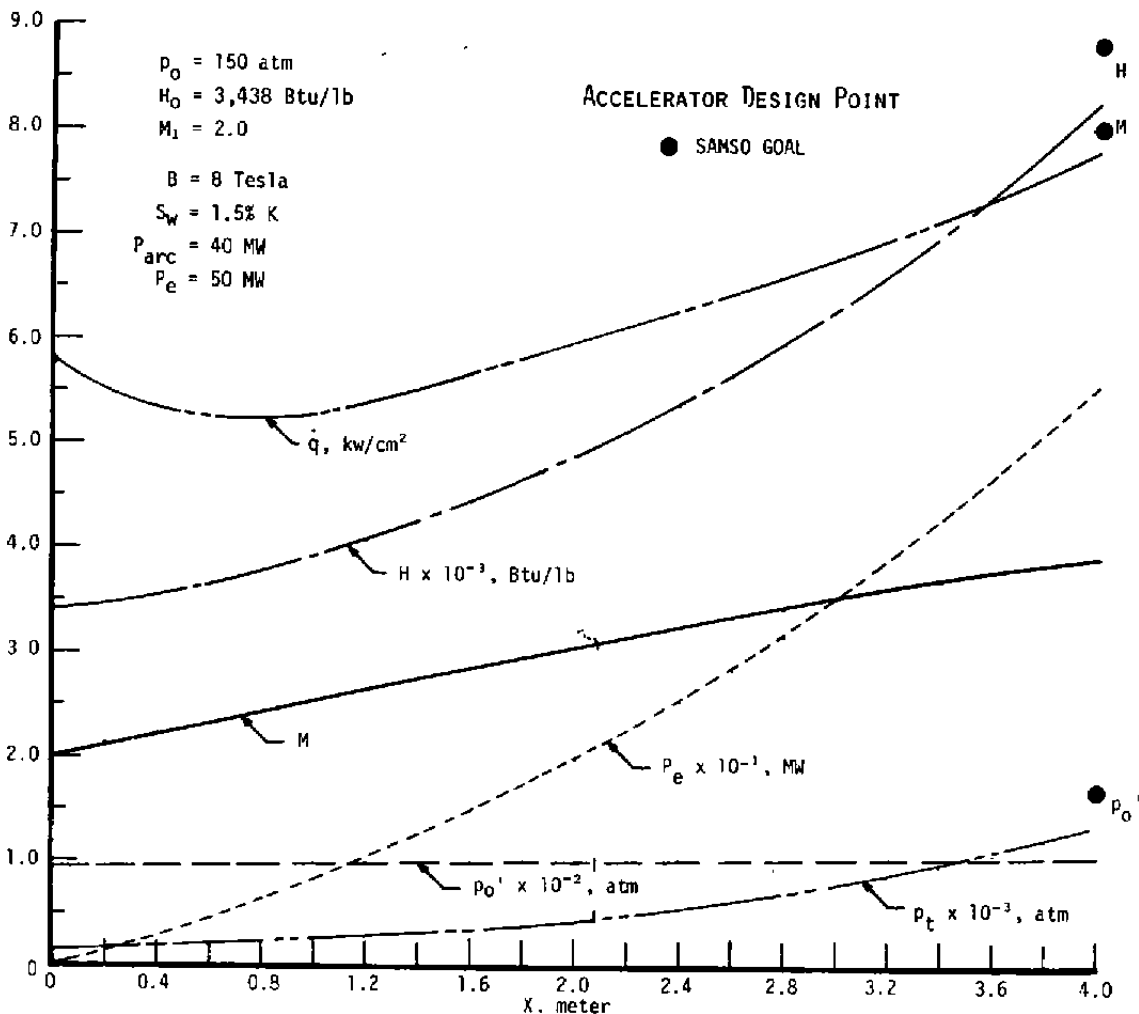

Figure 20. Typical accelerator performance plot.

Table 4. Summary of High-Power MHD-Accelerator Facility
Performance — Uncooled Walls

| | Parameter | Minimum Required Simulation | 50-MW Accelerator Plus Existing HEAT Facility | High-Power Accelerator Facilities | | | | |
				AEDC Power Limit Intermediate Future		AEDC Power Limit Ultimate		Ultra-High Power
MHD-Augmented Performance	P_e, MW		56	210	290	330	480	1,310
	P_0', atm	170.0	107	151	158	160	167	176
	M	8.0	3.9	5.1	5.4	5.6	6.0	6.8
	H, Btu/lb	8,800	8,300	12,700	13,500	18,500	20,300	23,600
	P_T, atm	---	1,350	10,000	14,600	26,000	40,000	100,000
	$\dot{Q}_w$, km/cm^2	---	7.8	10	11.5	12	14	14
	Exit Dimensions, in.	---	1.33 x 1.33	2.22 x 2.22	2.57 x 2.57	2.43 x 2.43	2.80 x 2.80	4.4 x 4.4
Arc Heater	P_0, atm		150	200 ⟶				
	H_0, Btu/lbm		3,348	3,500 ⟶				
	Power, MW		40	120	160	120	160	400
MHD Channel	B, Tesla		8	10 ⟶				
	Current, amp/cm^2		50	50 ⟶				
	Seed		1.5% K	1.5% K ⟶				
	M_{inlet}		2.0	2.0 ⟶				

Facility Configuration

The effect of arc heater performance on accelerator performance was investigated from the standpoint of chamber pressure and total enthalpy. Figure 21a shows the effect of enthalpy of a 200-atm arc heater on accelerator performance for the 50-MW power level, and Fig. 21b shows the same for a higher performance 300-atm arc heater. In Fig. 21b, the heat transfer and friction are deleted from the calculations to verify the trends with respect to enthalpy variation, and the performance shown on that plot is actually fictitious compared to a real case. In both instances, a slight increase in accelerator performance is shown as the supplied enthalpy increases. However, the increase is quite modest, confirming the belief that the arc heater need supply only enough energy to provide adequate seed ionization. Results of the studies indicate that enthalpies on the order of 3,500 Btu/lbm are adequate. This means that no ambitious arc development program will be required to provide a suitable plasma generator.

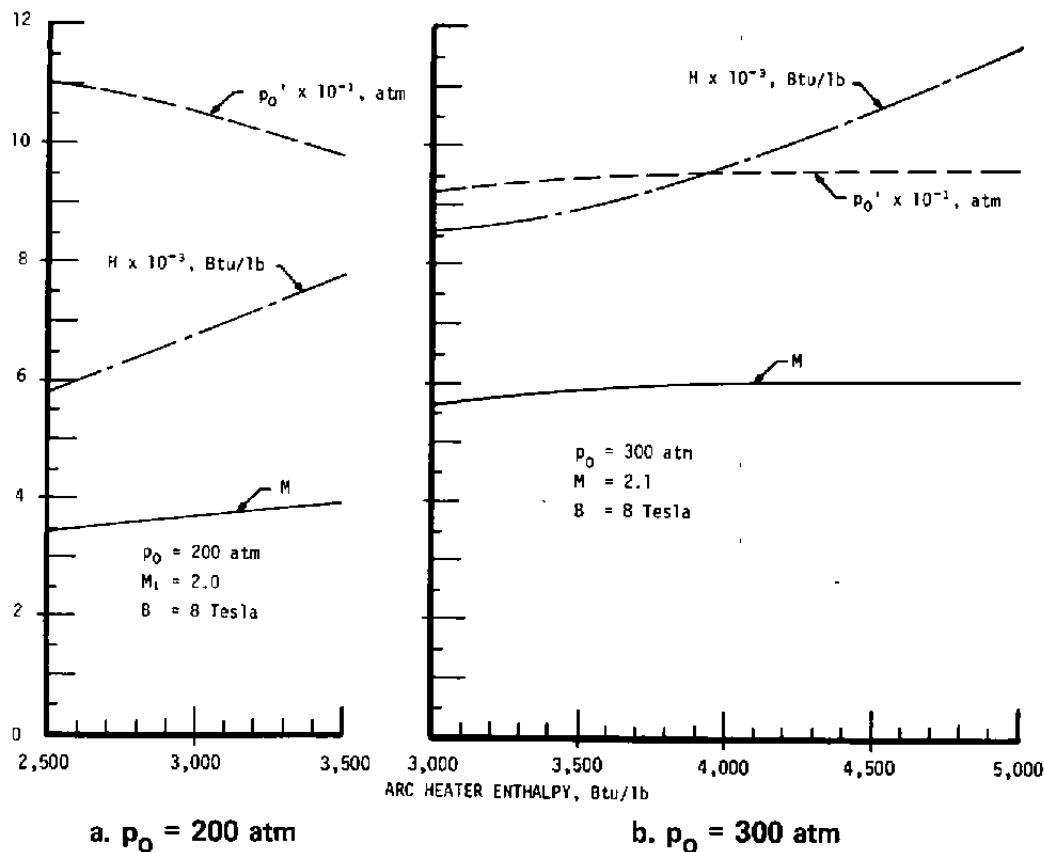a. p_o = 200 atm   b. p_o = 300 atm

Figure 21. Effect of arc heater enthalpy on accelerator performance.

The effect of arc heater total pressure on accelerator performance is shown in Fig. 22, where performance is shown to increase as the operating pressure is increased. Note specifically that the exit total enthalpy decreases somewhat as the supplied pressure increases, which tends to alleviate the excess enthalpy problem previously discussed. Since either Mach number or impact pressure can be acquired at the expense of the other, the stream total pressure is also shown in Fig. 22 and provides a more conclusive indication of increased performance. In general, then, the highest practical arc chamber pressure is desired. As the accelerator size is increased (higher power level, higher mass flow, larger physical size) the higher chamber pressures are also required to provide the required Reynolds number for model boundary-layer transition. Since only moderate enthalpies are required, the attainment of 300- to 400-atm chamber pressure is within near-term technology limits.
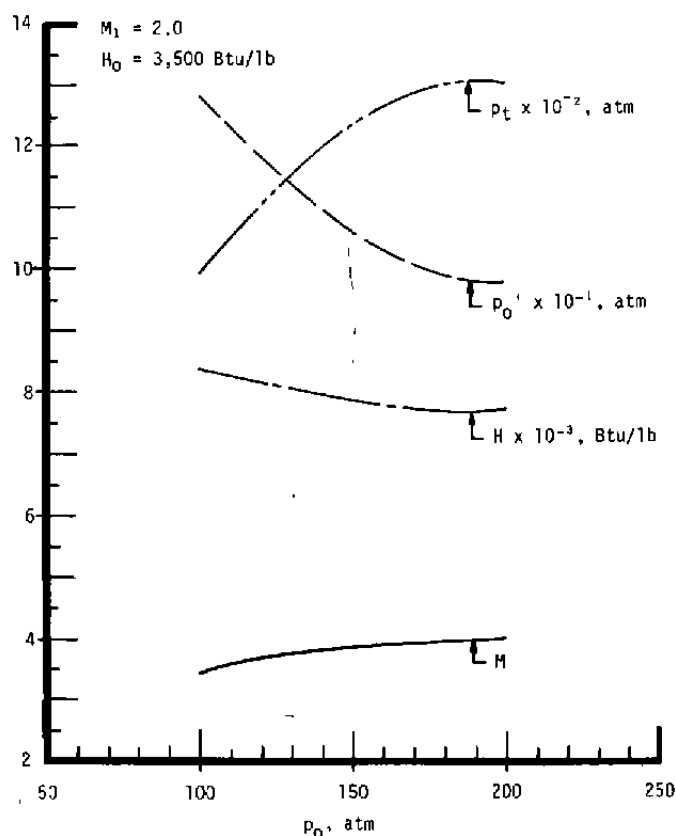

Figure 22. Effect of arc chamber pressure on accelerator performance.

57

With the arc heater conditions determined, a matrix of solutions was generated by varying channel inlet parameters. Figure 23 shows a typical variation of channel performance versus inlet Mach number for three enthalpy levels and p_0 = 200. The performance is relatively insensitive to inlet Mach number up to near 2.2. The degree of expansion allowed is essentially dependent on the required inlet conductivity, and the conductivity decreases quite rapidly as the inlet Mach number increases. The accelerator channel is somewhat self-governing, however, in that a low conductivity leads to high ohmic heating in the inlet region which tends to raise the temperature back to higher values. This is accomplished at the expense of input power, since a higher fraction of the energy is added as heat energy. For a given power level, then, the performance is somewhat reduced. The optimum inlet Mach number depends to some extent on the arc heater chamber conditions, of course, but in general is on the order of M = 2 for a properly matched arc heater and accelerator channel.
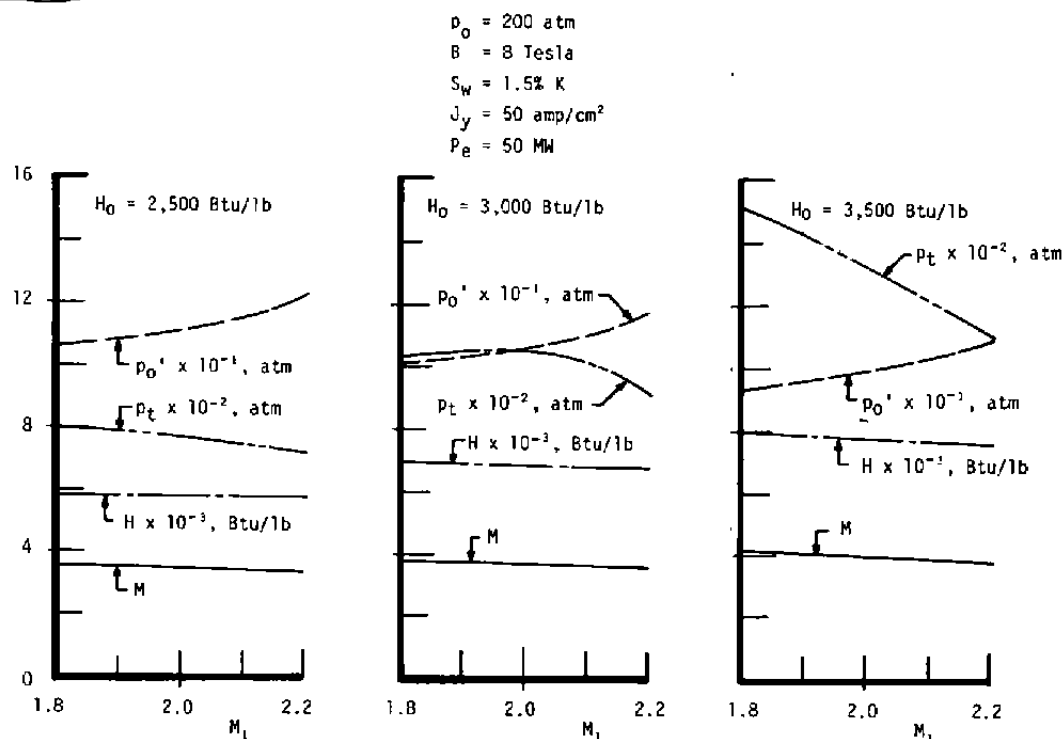

Figure 23. Effect of inlet Mach number on accelerator performance.

Studies were also conducted on the effect of magnetic field strength, seed rate, seed compound, and current density. As anticipated, the performance is strongly dependent on B-field as later plots will indicate. Data shown thus far has assumed a field strength of 8 T, assumed to be within the state of the art. A 10-T field would increase the performance, but requires a higher input power to drive an equal current density, since the applied voltage must overcome the uB term to force positive current flow. For the 50-MW accelerator size, no design point was seriously considered using a 10-T field since all components were limited to the present state of the art.

The accelerator performance was found to increase as the current density (or power density) was increased. This was as expected, of course, and is mentioned only to note that current densities were assumed from 20 to 100 amp/cm^2. The majority of calculations were held to 50 amp/cm^2, or less, since it is generally conceded that higher current densities would lead to unacceptable electrode erosion.

Varying seed rates were used as program inputs, and 1.5-percent potassium by weight was found to be near optimum for the present conditions. The performance increase which could be gained by using cesium was also investigated and found to be quite modest. At pressures above 20 atm and at temperatures which will yield $\sigma > 100$ mho/m, the conductivity of cesium is only 10 to 20 percent higher than potassium.

Referring again to Fig. 20, it should be noted that the performance shown on that plot is for a nominal 50-MW accelerator of near optimum configuration. Increasing the arc chamber pressure to 200 atm would increase the performance by a few percent, but not enough to warrant the increased difficulty with the existing arc heater operation. For an accelerator in this range, then, the test capability advantage over existing test units is significant but cannot approach the desired test conditions.

The wide margin between the desired test conditions and that which can be delivered by a 50-MW accelerator prompted the extension of the

59

present studies to high power levels and maximum magnetic fields, and results are tabulated in Table 4. Figure 24 shows the results of a typical sequence. This particular sequence of solutions was selected because it represents a significant size and power increase over the previous one, and falls generally in the midrange of power availability at AEDC in the foreseeable future. The results show Mach number on the order of M = 5 where hypersonic phenomenon should be observed. The two plots on Fig. 24 differ only in size, where the second plots shows a 33-percent increase in arc heater size. The resulting Mach number and impact pressure still fall below the desired minimums, even at these high power levels, and emphasizes the enormity of the effort required to reach such stringent conditions. Note also that the enthalpy is now significantly higher than the desired level, and attempts to increase Mach number tend to further increase the enthalpy level.

$$M_{min} \sim 8 \quad (T-1) \quad P_{min} \sim 170 \, \overline{d}$$

$$M_{req} \sim 20 \quad P_{req} \sim 200 \, d$$

$$p_0 = 200 \text{ atm}$$
$$M_i = 2.0$$
$$H_0 = 3,500 \text{ Btu/lb}$$
$$S_w = 1.5\% \text{ K}$$
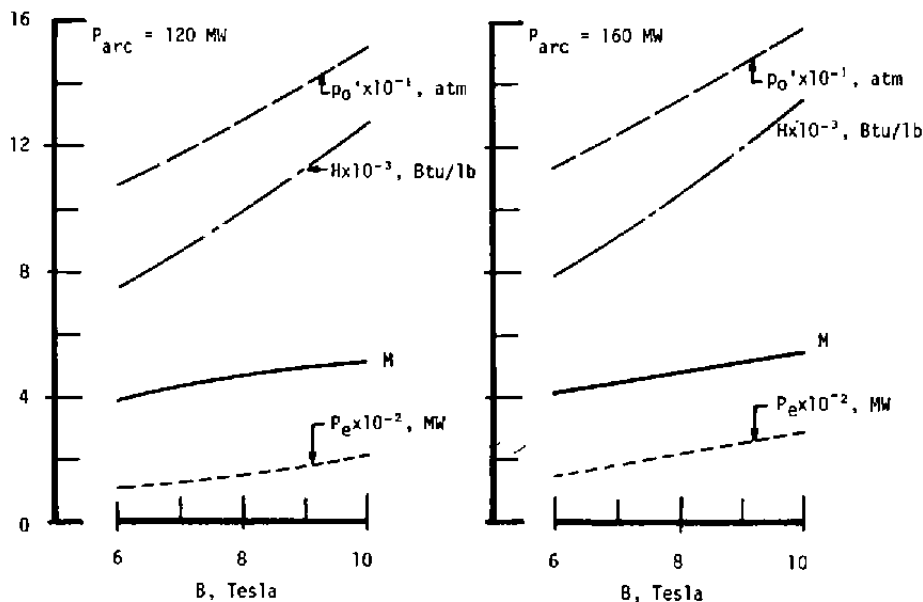$$J_y = 50 \text{ amp/cm}^2$$

Figure 24. Accelerator performance for 300-
to 400-MW system.

At these higher power levels, the power requirement can now be discussed in more detail. As shown in Fig. 24, the power requirement varies almost linearly with B-field. The solutions have assumed a tailored current density, constant down the channel. For a uniform magnetic field then, the accelerating force, jxB, is constant at each point in the channel. The applied voltage must supply the prescribed current density, after overcoming the opposing induced voltage uB. That opposing voltage, of course, varies linearly with B, and the applied voltage must be increased uniformly down the channel. It might be further noted that the rate of power addition increases down the channel, with the majority of the power added toward the channel exit. This simply stems from the fact that if successful velocity increase is achieved, uB becomes even higher. Therefore, the higher the velocity, the higher the power required to further accelerate the flow. The variation in plasma conductivity will affect the linear relations somewhat but cannot alter the trend. In general, the conductivity will increase down the channel. Calculations have shown that a constant temperature channel yields near optimum results, and since the static pressure must always decrease, the conductivity will increase.

Figure 25 shows accelerator performance with respect to magnetic field at yet higher power levels. The arc drivers are the same as in Fig. 24, only a longer channel (5 m) is assumed. The combined accelerator and arc heater power for this case is approaching the maximum anticipated installed capacity at AEDC. Increased performance is noted, but the enthalpy mismatch is approaching an intolerable level. Note that the impact pressure is approaching the desired value of 170 atm, and the Mach number is high enough to produce most hypersonic phenomena. Even with the total available power, however, the full simulation is not achieved.

Finally, Figure 26 shows a typical run at extremely high power levels, driven by a 400-MW arc heater. The impact pressure and Mach number are duplicated, but the total enthalpy is three times the desired level. The maximum total power for such a system is 1,700 MW, clearly above the level which could reasonably be proposed.

$BTU \times .3 = whr$

$40 MW = 1.3 \times 10^8 \frac{BTU}{L}$

$\rightleftharpoons n \cdot 2 z$

$$p_0 = 200 \text{ atm}$$
$$M_1 = 2.0$$
$$H_0 = 3,500 \text{ Btu/lb}$$
$$S_w = 1.5\% \text{ K}$$
$$J_y = 50 \text{ amp/cm}^2$$
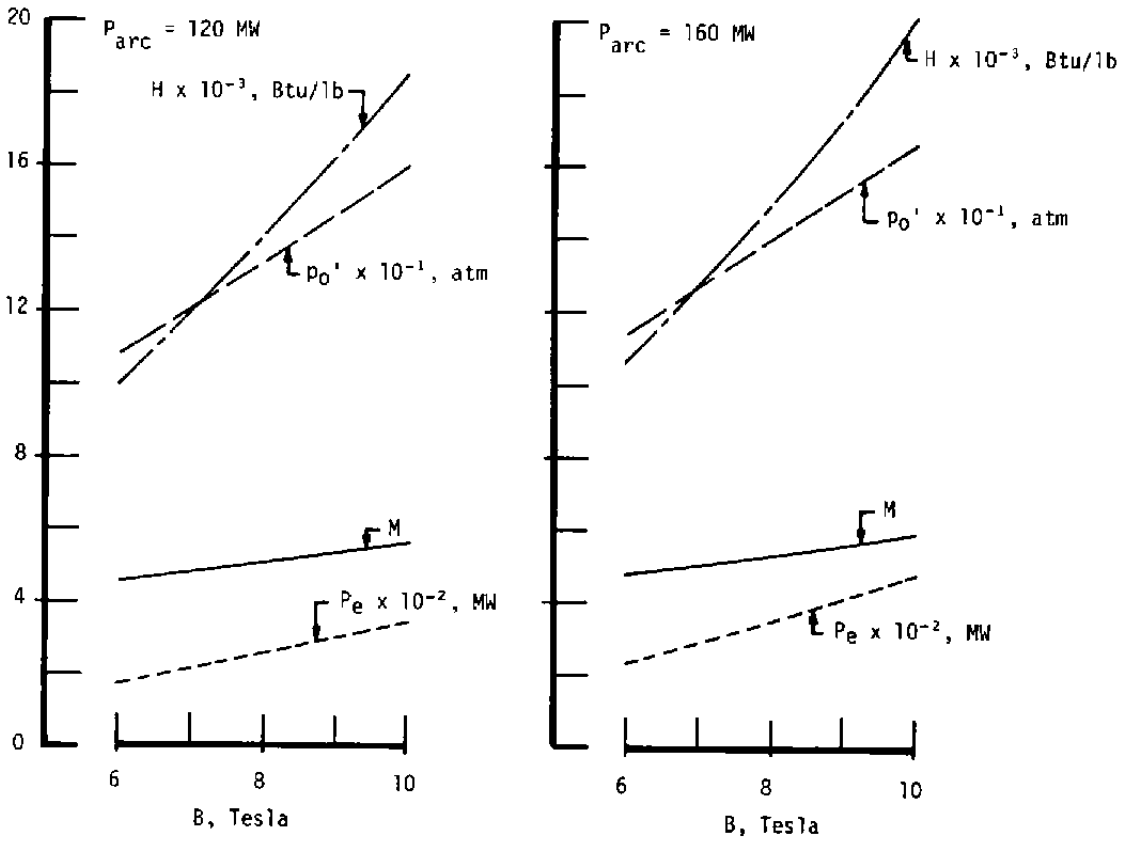
Figure 25. Accelerator performance at increased power levels.
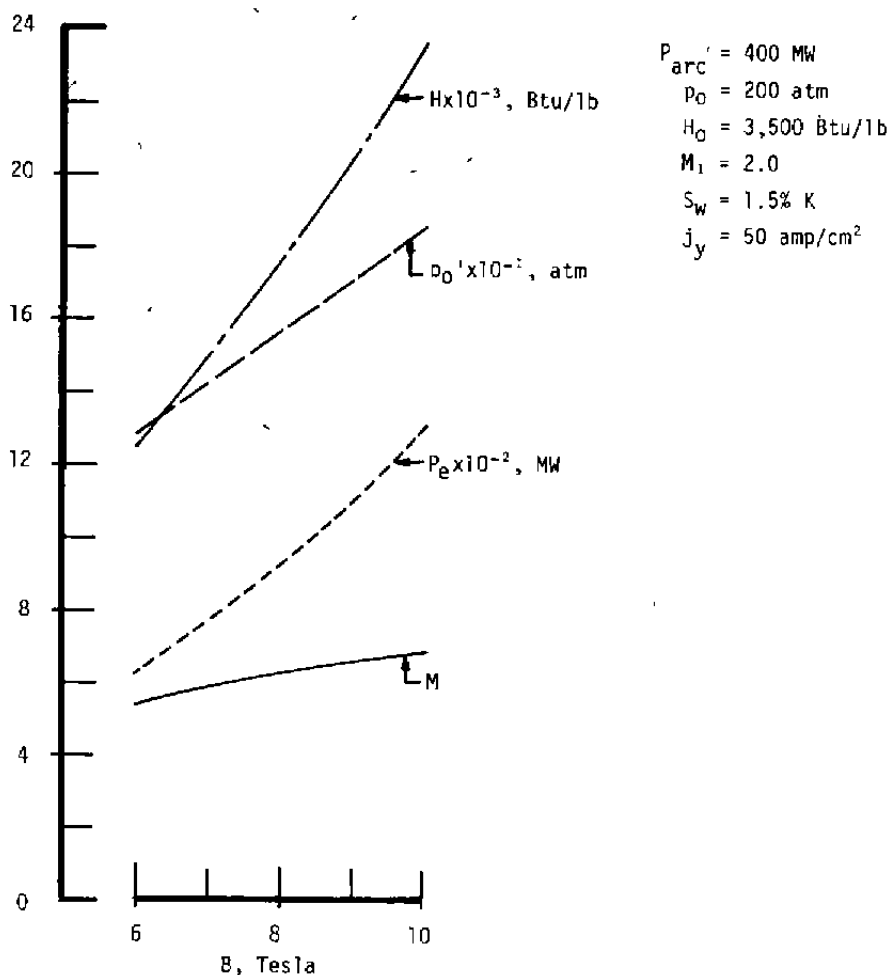
Figure 26. Accelerator performance using
400-MW arc heater.

The analytical data shown have only hinted to this point about the extremely high heat-transfer rates in the accelerator channel, and it has been assumed that a properly designed channel could sustain such heat loads. Figure 20 gives the heat-transfer rates down the channel for the 50-MW channel, and Fig. 27 gives the same for a higher power level. Figure 27 shows the other parameter variation as well, and is the axial plot of the 10-T point on the 120-MW arc of Fig. 24. In Fig. 20, the maximum heat load approaches 8 kw/cm^2 and as higher performance is required,
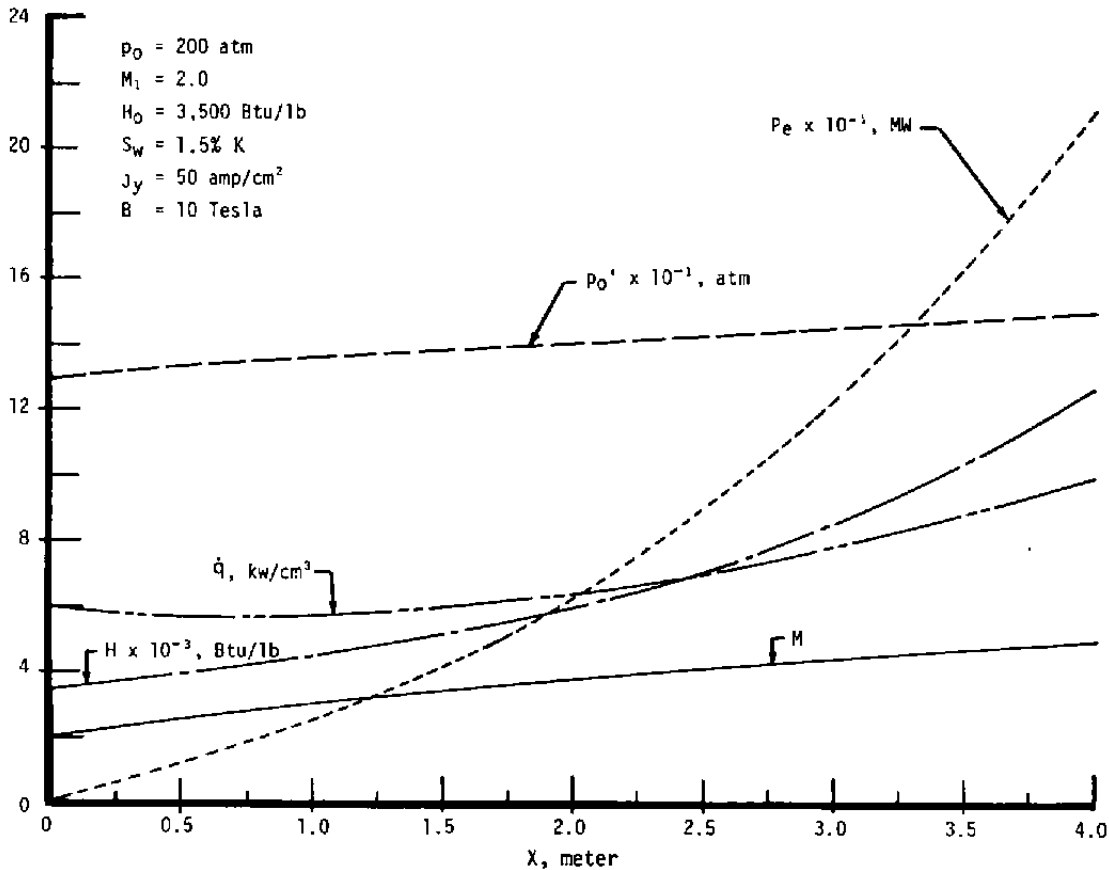
Figure 27. Variation of accelerator parameters as a function of channel distance.

the heat load increases, up to 10 kw/cm^2 in Fig. 27. Even higher heat-transfer rates were obtained for the very high power solutions, up to a maximum of 14 kw/cm^2. A literature search and discussion with various manufacturers of insulator materials resulted in the conclusion that existing insulator materials are inadequate to withstand such severe conditions. Previous accelerator programs have utilized alumina or beryllium oxide as insulator wall materials, and those materials remain as the most attractive possibilities in the near future. Some advances have been made in the temperature limits of those materials since last employed in accelerator channels, but the advances have been minimal. The maximum-use temperature for both materials is on the order of 1,900°K;

both fail under no-load conditions at higher temperatures. Furthermore, beryllia poses additional problems because of its toxic nature.

Other, newer materials were also investigated, including the ceramic-metal composites. Materials development will undoubtedly result in more attractive insulators, but the present technology level is below the present requirements. Based on present insulator materials capability, it is doubtful that existing materials can withstand such severe conditions. For that reason, the possibility of using film cooling of the insulated B-walls was investigated and the results of that study are discussed in Section 7.0.

7.0 RESULTS OF FILM COOLING STUDIES

As discussed in Section 5.0, the feasibility of film cooling the B-walls of an accelerator channel was conducted using a two-dimensional code modified to incorporate the MHD effects. The solutions were obtained for conditions previously analyzed so that comparative performance values were generated. The solutions assumed a film of cold air of specified thickness to be added tangentially to the main flow, with additional thin film injections made each time the wall reached a specified temperature. Each time a film was added, the channel width was increased to maintain the same core flow area across the injection point. The channel aspect ratio varied, therefore, depending on the amount of film cooling added down the channel.

Figure 28 gives the results of the solution where the inlet conditions were identical to those shown in Fig. 20. The accelerator performance parameters are plotted, as well as the mass flow ratio, which show the magnitude of film coolant in the flow. These solutions were, again, generated with a specified current density across the channel and a specified B-field, both being the same as used in Fig. 20. Therefore, the body force per unit volume on the channel centerline was equal to that in the uncooled solution. Note, then, from the summary tabulation, Table 5, that the Mach number at the exit remained high, and likewise the impact pressure. Continual mixing decreased the flow enthalpy by 30 percent, well
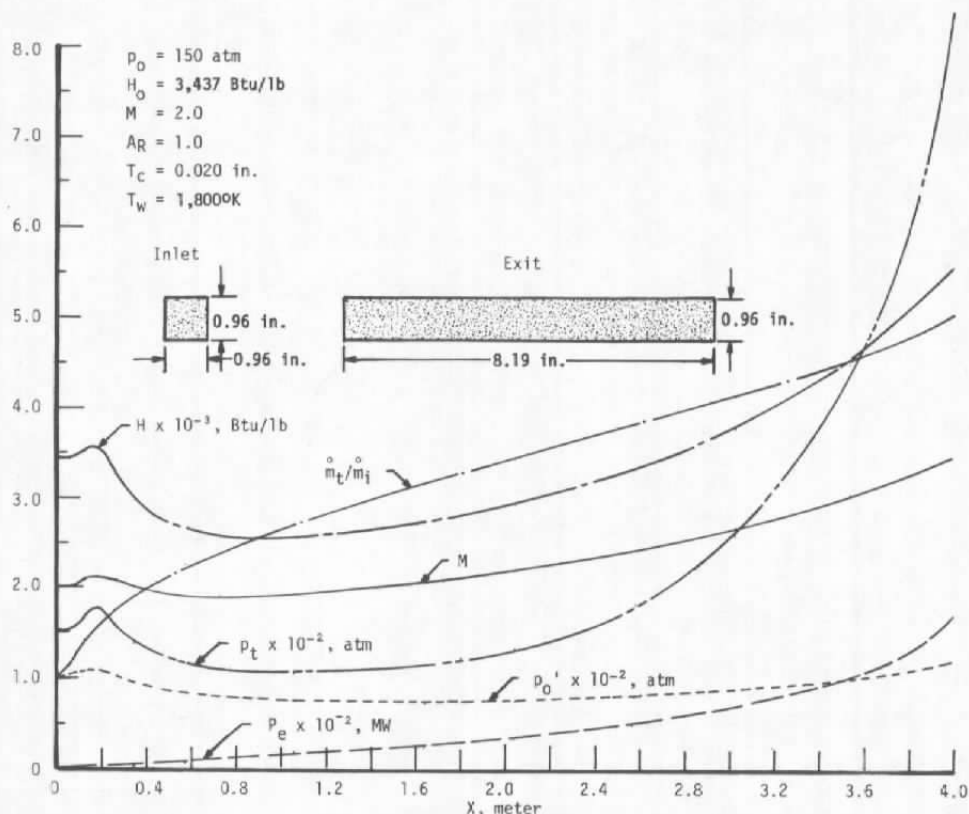
Figure 28. Accelerator performance with film-cooled sidewalls.

below the previous value. The most significant result, however, was the volume of film cooling required. The final mass flow in the solution shown was five times the inlet flow. As a direct result of that parameter, the power required to produce the exit performance is shown to be 170 MW as compared to the 50 MW in the uncooled original solution. The total enthalpy profile gives the best indication of the physical results. The enthalpy initially increases as in the uncooled case, but as repeated films are added the film cooling mixes with the hot core, thereby reducing the centerline enthalpy. The conductivity is also reduced, leading to high ohmic heating rates. The predominant fraction of added energy is added as heat rather than acceleration. Continued cool air addition further reduces the bulk enthalpy, thereby reducing the heating rate to

Table 5. Summary of High-Power MHD-Accelerator Performance-Film-Cooled B-Walls

	Parameter	50-MW Accelerator Plus HEAT Facility (Uncooled)	Variable Aspect Ratio		Constant Aspect Ratio	
			Nonoptimized Cooling (Fig. 28)	Optimized Film Cooling	Film-Cooled Accelerator + HEAT Facility	Large Facility
MHD-Augmented Performance	P_c, MW	56	167	165	120	705
	$P_o{}'$, atm	108	120	150	115	140
	M	3.9	3.45	4.0	3.35	3.95
	H, Btu/lbm	8,300	5,600	6,500	5,530	6,850
	P_T, atm	1,350	840	1,200	690	1,200
	$\dot{Q}_w$, kw/cm^2	7.8	----	----	----	----
	Exit Dimensions, in.	1.33 x 1.33	0.96 x 8.19	0.679 x 7.2	1.94 x 3.88	3.12 x 6.24
Arc Heater	P_o, atm	150	150 ⟶			190
	H_o, Btu/lbm)	3,438	3,438 ⟶			3,490
	P_{heater}, MW	40	40 ⟶			80
MHD Channel	B, Tesla	8	10 ⟶			
	Current, amp/cm^2	50	50 ⟶			
	Seed	1.5% K	1.5% K ⟶			
	M_{inlet}	2.0	2.0 ⟶			
Film Cooling	T_c, in.		0.020	0.01	0.010	0.010
	T_w, °K		1,800	2,000	2,200	1,800
	$\dot{m}_t/\dot{m}_i$		5.0	3.55	4.85	3.35
	A_R Inlet		1.0	0.5	0.5	0.5
	A_R Exit		0.117	0.168	0.5	0.5

Facility Configuration

67

the wall, requiring less film coolant, until the lower equilibrium condition is achieved. The kinetic enthalpy, $u^2/2$, continues to increase until that enthalpy increase plus the higher ohmic heating begins to increase the total enthalpy and continues to do so but at the expense of high power addition.

Since the channel walls are expanded each time an air film is added, the extremely high mass addition leads to channels with extremely low aspect ratios. That condition is undesirable and will be further discussed later.

The data in Fig. 28 assume a cooling film thickness of 0.020 in. The effect of decreasing the film thickness, at the expense of more injection points, was investigated. Figure 29 shows the results of the calculations assuming the same accelerator inlet conditions as before. That plot indicates that a significant decrease in the amount of film coolant can be achieved by reducing the film thickness. It is postulated that extrapolation of that curve to zero film thickness would simulate a porous wall condition, the limiting case for discrete location injection. The existing code is incapable of addressing the porous wall case, however, and discrete injection was used throughout the study. Note that a reduction in film thickness to 0.010 in. reduces the mass addition by 20 percent.

Since the electrode walls are assumed to be cooled by backside cooling, the possibility of increasing the electrode wall area and decreasing the insulator wall area at the inlet was investigated. This is simply equivalent to reducing the wall areas to be film cooled. Those results are also shown in Fig. 29, and show an additional 20-percent decrease in the required mass addition. The wall temperature limit which triggers the film injection was set at 1,800°K for the data presented, a value considered relatively safe. The high mass fraction addition prompted a quick look at the effect of increasing that limit, with those results also shown in Fig. 29. A slight reduction in mass addition is shown in that figure, where the decreased film thickness and

aspect ratio have been included. The wall failure limit corresponds to published temperature limits on high grade alumina and beryllium oxide insulators. As can be seen, the mass fraction addition still remains near three, which means that twice the original mass flow is added as coolant, still unacceptably high.
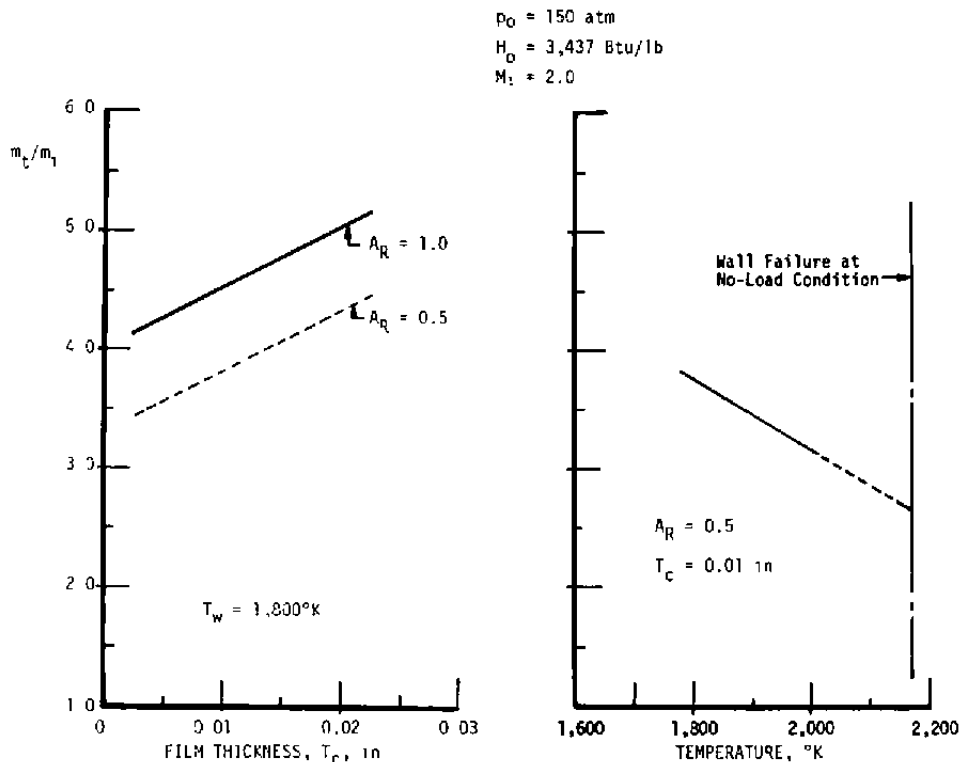
Figure 29. Effect of film thickness, aspect ratio, and wall temperature on coolant mass.

Figure 30 indicates the overall effect on channel performance by decreasing the film thickness, decreasing the aspect ratio, and increasing the allowable wall temperature as suggested by Fig. 29. The mass ratio at the exit is near three as predicted. The solid symbols indicate the performance previously shown in Fig. 28. The predicted increase in performance is clearly noted, but still falls short of the performance shown for the corresponding uncooled case of Fig. 20. The power level is approximately triple the uncooled case, indicating that

$u_e \simeq 50\sqrt{T} = 50\sqrt{3600} = 3000 \ f/s \qquad A_e = \frac{7.2(.679)}{144} \simeq 3.4 \times 10^{-2} \ sf$

$\rho_e = \frac{\dot{m}_\theta}{u_e A_e} = \frac{23}{3000(.034)} \simeq 0.23 \ \#/cf \simeq 0.12 \ \#/cf \ @ \ P_r \sim 50\% ?$

the film cooling is still dominating the channel characteristics, but
a higher fraction of the power has gone into accelerating the flow
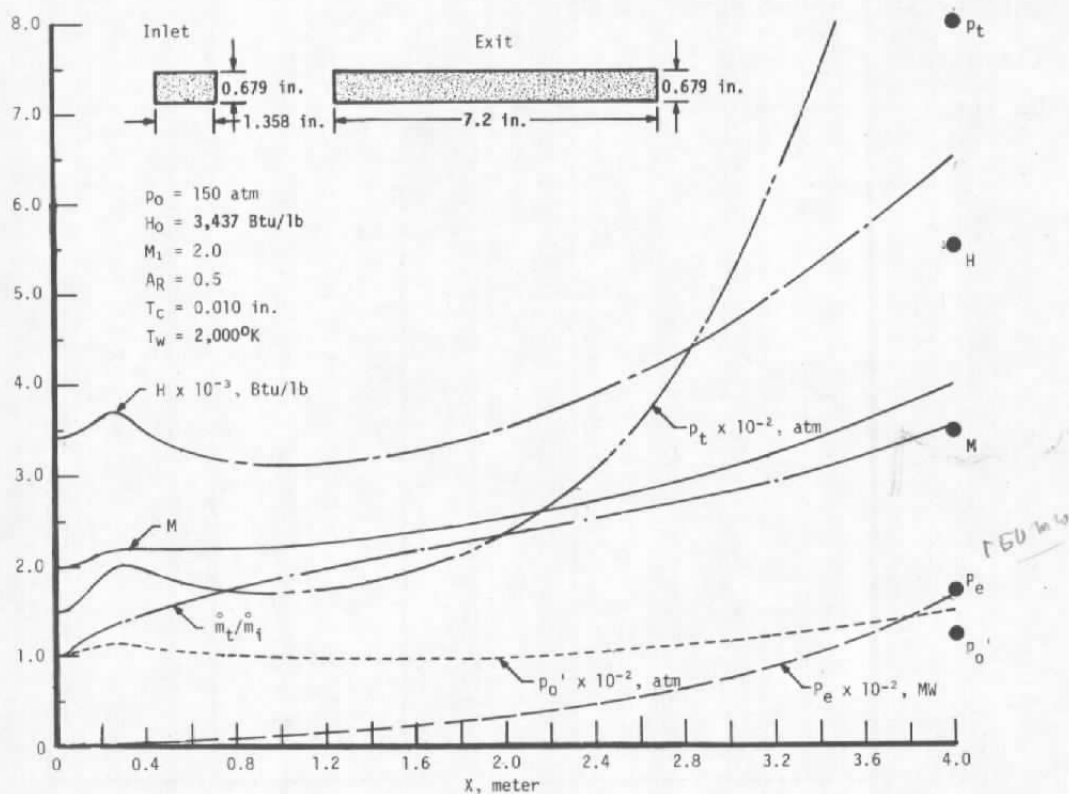than in Fig. 28. The exit aspect ratio is also still undesirably low.

**Figure 30. Film-cooled accelerator performance
with optimum variables.**

Although the penalty in power requirement is recognized, an objective
analysis of the performance shown in Fig. 30 indicates a substantial in-
crease in capability over existing test unit, and is equivalent to expan-
sion from a 1,200-atm reservoir at moderately high enthalpy. The undesir-
able aspect ratio could possibly be modified by altering the flow at the
exit to produce a more useful test rhombus. The flow conditioning would
be fairly drastic, however, and flow nonuniformities might be unacceptable.

To circumvent the low aspect ratio difficulty, solutions were obtained
retaining the advantage of the reduced aspect ratio at the channel inlet,

$P_e = 150 \ mw \sim 1.5 \times 10^5 \ kw \sim 1.5 \times 10^5 \ BTU/s$

$H_\theta \sim 6.5 \times 10^3 \ BTU/\#$

70

$\therefore \ P_e/H_e \simeq \frac{150}{6.5} \simeq 23 \ \#/s \simeq \dot{m} \simeq 12 \ \#/s \ @ \ 50\% \ off \ of \ P_e$

but maintaining that ratio as constant down the channel. Figure 31 shows the resulting performance to be reduced significantly, essentially equivalent to the results shown in Fig. 28 except for the more desirable test rhombus and the lower power requirement. The reduction in power requirements stems from the fact that with the constant A/R the conductivity profile across the channel is much less severe, resulting in a reduction in the required applied voltage.
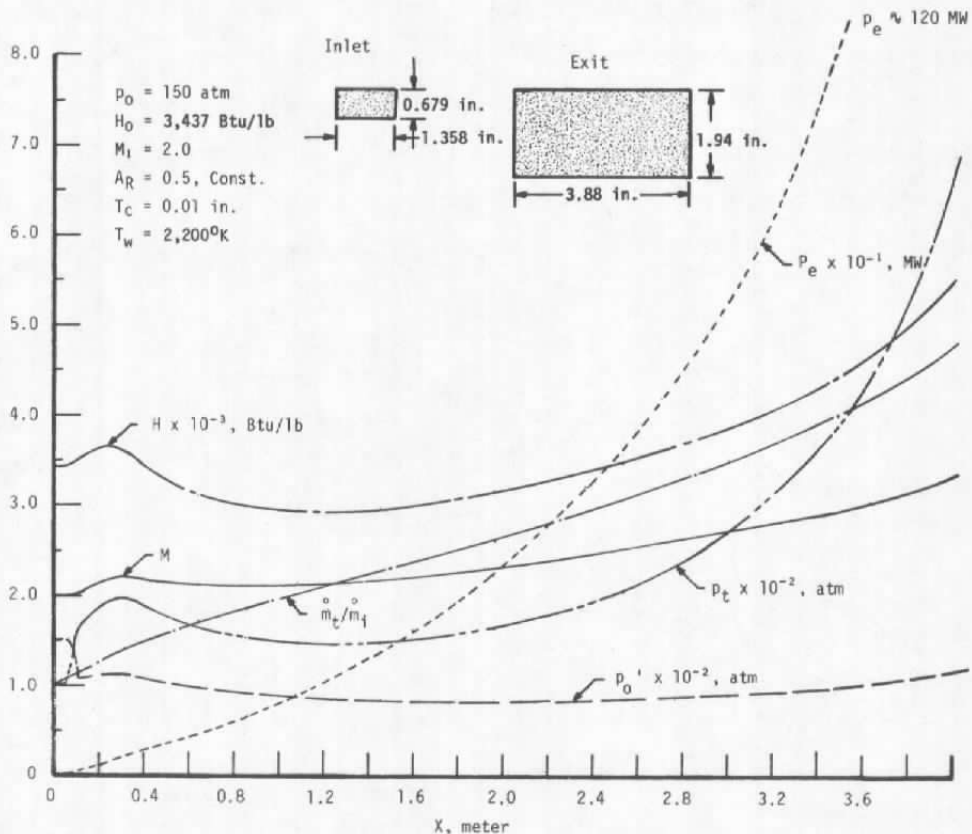
Figure 31. Film-cooled accelerator performance with constant aspect ratio.

Finally, additional solutions were obtained to determine the possible increase in performance which could be obtained by an increase in accelerator size, where the higher flow area to wall area ratio might prove beneficial. Figure 32 shows the results of one such solution. The channel in this case was powered by an 80-MW arc heater, but the resulting mass flow

71

at the channel exit, including film cooling mass, is equivalent to a 250-MW heater driving an uncooled channel. The overall performance is quite desirable, but the power level is seen to be on the order of 700 MW. That power level is near maximum for anticipated capacity at AEDC. In view of the fact that the calculated performance is much lower than the desired goals, the cost for such a system is considered to be unacceptably high.

The results of the film-cooled study are summarized in Table 5. It can be seen that the optimized film-cooled solutions corresponding to the uncooled case have considerably less desirable performance, even at higher power levels. To achieve near equivalent performance, one must increase the power level in the cooled channel by an order of magnitude as shown in the last set of data. The use of film cooling to overcome the high heat loads to the insulator walls does not appear to be promising.
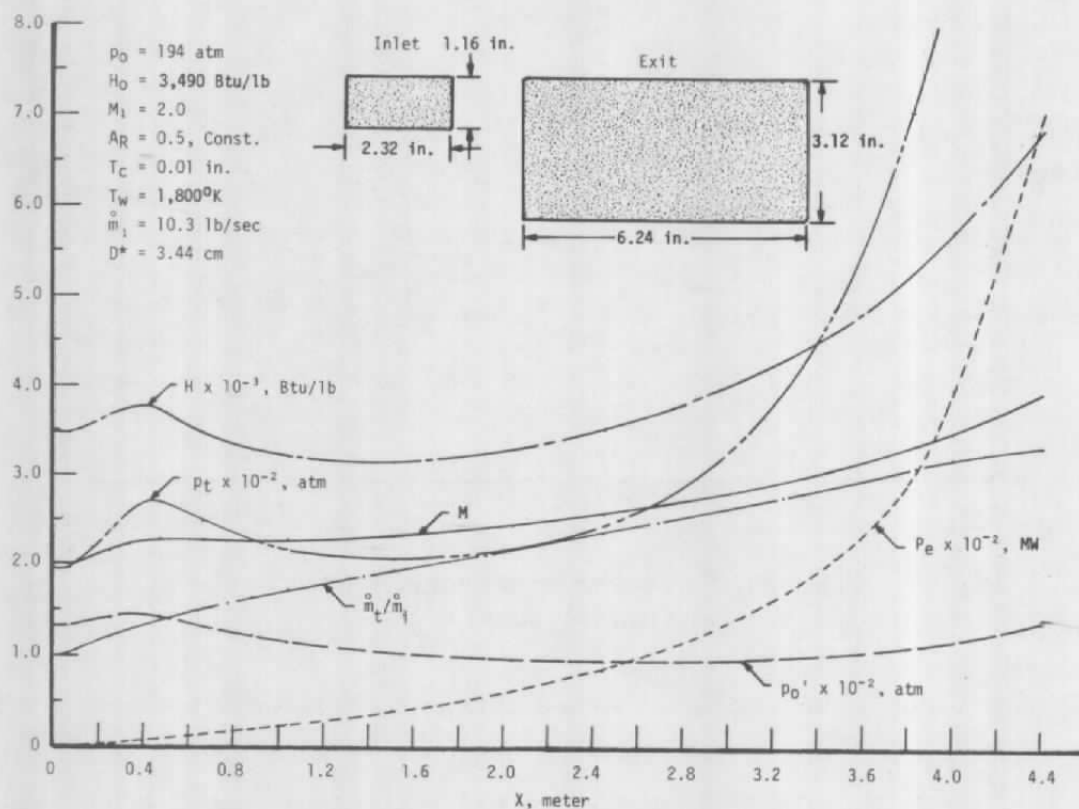

Figure 32. Performance of large film-cooled accelerator.

8.0 CONCLUDING REMARKS

The development of a large-scale ground test facility which will duplicate the conditions experienced by a ballistic missile reentering the earth's atmosphere poses formidable obstacles. So stringent are the requirements that full simulation is impossible to attain in a conventional fixed-model facility. Analytical calculations have indicated that significant improvement in the present test capabilities can be achieved by the use of an MHD-augmented arc facility, but those same studies have revealed that major technological advances would be required to successfully develop such a system. An augmented arc system on the order of 100-MW total input power would deliver a test stream of M = 3.9 at an impact pressure of 107 atm and total enthalpy of 8,000 Btu/lbm. The power requirement is within the presently installed capacity at AEDC. A 600-MW system, essentially equivalent to the future installed capacity at AEDC, would deliver M = 6 at 160 atm, but at enthalpy levels twice that desired. Finally, a 1,700-MW system would deliver flow streams which effectively simulates the Mach number and impact pressure, but at triple the desired enthalpy. In each case, however, the heat-transfer rates to the channel wall are excessive, and it is doubtful the existing materials can withstand the severe environment. The film cooling studies indicate that significant reduction in performance will accompany any attempts to film cool the insulator walls, and power requirements would become very large.

The comprehensive studies suggest that a major development effort would be required to develop an MHD-augmented arc facility. Previous experimental work cannot be extrapolated into the present operating regime, and the development effort would require a graduated effort of several years' duration with major funding commitment. Significant increases in high-temperature materials technology, however, would have a large effect on these conclusions.

REFERENCES

1. Trimble, M. H., Smith, R. T., and Matthews, R. K. "AEDC High Temperature Testing Capabilities." AEDC-TR-78-3 (ADA053150), April 1978.

2. Derbidge, T. C. and Wolf, C. J. "Comparative Analysis of Technical Performance and Cost Benefits of Reentry Vehicle Ground and Flight Test Facilities." AEDC-TR-77-127 (ADB024498L), January 1978.

3. Rittenhouse, L. E., Pigott, J. C., Whoric, J. M., and Wilson, D. R. "Theoretical and Experimental Results with a Linear Magnetohydrodynamic Accelerator Operated in the Hall Current Neutralized Mode." AEDC-TR-67-150 (AD385365), November 1967.

4. Rittenhouse, L. E., Whoric, J. M., and Pigott, J. C. "Experimental Results with a Linear Magnetohydrodynamic Accelerator Operated with Water-Cooled Beryllia Magnetic-Field Walls." AEDC-TR-70-40 (AD508164), April 1970.

5. Carter, A. F., McFarland, D. R., Weaver, W. R., Park, S. K., and Wood, G. P. "Operating Characteristics, Velocity, and Pitot Distribution, and Material Evaluation Test in the Langley One-Inch-Square Plasma Accelerator." Paper presented at AIAA Plasmadynamics Conference, Monterey, California, March 2-4, 1966.

6. Hilsenrath, Joseph and Klein, Max. "Tables of Thermodynamic Properties of Air in Chemical Equilibrium Including Second Virial Corrections from 1,500°K to 15,000°K." AEDC-TR-65-58 (AD612301), March 1965.

7. Schneider, R. T. and Wolfer, W. G. "Nomogram for Saha's Equation." Prepared under Contract Nonr-580(19) by the University of Florida, Gainesville, Florida, March 1967.

8. Friel, P. J. "Electron Density and Electrical Conductivity of High Temperature Air Seeded with Alkali and Alkaline Earth Metals." General Electric Document No. R59SD459, December 1959.

9. Chapman, Sydney, and Cowling, T. G. The Mathematical Theory of Non-Uniform Gases. Cambridge University Press, Cambridge, England, 1958.

10. Spitzer, L., Jr., and Härm, R. "Transport Phenomena in a Completely Ionized Gas." Physical Review, Vol. 89, No. 5, March 1953, pp. 977-981.

11. Shkarofsky, I. P., Bachynski, M. P., and Johnston, T. W. "Collision Frequency Associated with High Temperature Air and the Scattering Cross Sections of the Constituents." RCA Victor Company Research Report No. 7-801, March 1960.

12. Lin, S. C., Resler, E. L., and Kantrowitz, A. "Electrical Conductivity of Highly Ionized Argon Produced by Shock Waves." Journal of Applied Physics, Vol. 26, No. 1, January 1955, pp. 95-109.

13. Demetriades, S. T. and Argyropoulos, G. S. "Ohm's Law in Multi-component Nonisothermal Plasmas with Temperature and Pressure Gradients." The Physics of Fluids, Vol. 9, November 1966, pp. 2136-2149.

14. Patankar, S. V. and Spaulding, D. B. Heat and Mass Transfer in Boundary Layers, 2nd Edition, CRC Press, Cleveland, Ohio, 1970.

15. Kessel, P. A. "A Study of the Aerodynamic Design of Viscous Nozzles Used to Accelerate Large Particles to High Velocities." PhD Dissertation, University of Tennessee, Knoxville, Tennessee, March 1977.

16. Lieu, B. H. "Air Film Cooling of a Supersonic Nozzle." NOL TR-64-65, U. S. Naval Ordnance Laboratory, White Oak, Maryland, August 1964.

17. Williams, John. "A 7T Superconducting Magnet for MHD Studies at Stanford University." Final Design Report, Francis Bitter National Magnet Lab, November 1977.

18. Williams, John E. C. "Superconducting MHD Magnet Development Program." Annual Progress Report No. 1, Francis Bitter National Magnet Lab, December 1977.

NOMENCLATURE

A	Area, m^2
A^+	Damping constant in Van Driest's hypothesis
AR	Channel cross-section aspect ratio
a	Speed of sound, m/sec
B	Magnetic field strength, Tesla
c_f	Friction coefficient
D	Diameter
D_h	Hydraulic diameter, m
E	Electric field, v/m
E*	Effective driving field, v/m
E_H	Hall field, v/m
e	Electron charge, 1.602×10^{-19}, coulomb
H	Total enthalpy, Btu/lbm or joule/kg
H_o	Reservoir enthalpy, Btu/lbm or joule/kg
h	Static enthalpy, Btu/lbm or joule/kg
j	Current density, amp/cm^2
k	Turbulence model constant
L	Total length, m
ℓ	Turbulence model mixing length
M	Mach number
$\dot{m}$	Mass flow rate, kg/sec
n_e	Electron number density, $1/m^3$
Pr	Prandtl number

p   Static pressure, Nt/m^2 or atm

P_e Electric power, MW

P_o' Impact pressure, atm or Nt/m^2 — *total press. downstream of normal shock*

P_t Total pressure, atm or Nt/m^2

q   Heat-transfer rate to channel walls, kw/cm^2

R   Gas constant, joule/kg $^\circ K$

RV   Reentry vehicle

R_N Nose radius, in.

r   Distance from wall

r_ℓ Characteristic boundary-layer thickness

S   Entropy, joule/kg $^\circ K$ or distance from stagnation point along cone surface

S_w Seed rate by weight

T   Temperature, $^\circ K$

U   Internal energy, joule/kg

u   Velocity in the x direction

V_e Reentry velocity, ft/sec

v   Velocity in the z direction, also specific volume, m^3/kg

x   Distance from channel inlet, m

Z   Compressibility factor

β   Angle between resultant electric field and flow direction, deg, also ballistic coefficient, lb/ft^2

γ   Reentry angle, deg

θ   Slant-wall angle, deg

θ_c Cone half-angle, deg

λ	Turbulence model constant
μ	Molecular viscosity
ξ	Transformed length variable, Eq. (57)
ρ	Density, kg/m^3
Σ	Wall shear stress gradient, $4 \tau_w/D_h$, $Newton/m^3$
σ	Electrical conductivity, mho/m
σ_{ei}	Electrical conductivity considering scattering by ions, mho/m
σ_{en}	Electrical conductivity considering scattering by neutral particles, mho/m
τ_w	Wall shear stress, $c_f(\rho u^2)/2$, $Newton/m^2$
φ	Ratio of E_y/E_x = Cot θ; also general dependent variable
ψ	Stream function, Eqs. (58) and (59)
ω	Nondimensional stream function, Eq. (60)
ωτ	Hall parameter

SUBSCRIPTS

c	Cooling
C_L	Centerline value parameter
e	Exterior
eff	Effective
i	Initial or interior
o	Total or reservoir conditions
t	Total
x	Parameter component in x direction

y   Parameter component in y direction

*   Sonic conditions

SUPERSCRIPTS

'   Turbulent fluctuations about an average

‾‾‾   Time average